A numerical framework for the simulation of coupled electromechanical growth

Zhanfeng Li[a,b], Chennakesava Kadapa[c,*], Mokarram Hossain[b,*], Jiong Wang[a,d,*]

[a] *School of Civil Engineering and Transportation, South China University of Technology, Guangzhou, 510640, Guangdong, China*
[b] *Zienkiewicz Institute for Modelling, Data and AI, Swansea University, Swansea, SA1 8EN, UK*
[c] *School of Engineering and the Built Environment, Edinburgh Napier University, Edinburgh, EH10 5DT, UK*
[d] *State Key Laboratory of Subtropical Building Science, South China University of Technology, Guangzhou, 510640, Guangdong, China*

Abstract

Electro-mechanical response exists in growing materials such as biological tissues and hydrogels, influencing the growth process, pattern formation and geometry remodelling. To gain a better understanding of the mechanism of the coupled effects of growth and electric fields on the deformation behaviour, a finite element framework for coupled electro-elastic growth is established. Based on the extended volume growth theory, the governing equations of the growing electro-elastic solid are obtained. A coupled three-field mixed displacement-pressure-potential finite element formulation using inf–sup stable combinations is adapted. The finite element formulation is implemented in ABAQUS via a user element subroutine. The implementation is validated first by comparing the deformation and stress components of a growing tubular structure under axial strain and radial voltage. Using the example of a bi-layer beam actuator, it is illustrated that growth parameters and the external voltage can precisely control the bending angle. The framework is then applied to simulate pattern formation and transition behaviour, such as doubling and tripling of wrinkles, by specifying growth parameters and external voltage in a 3D stiff film/soft substrate structure. Furthermore, the suppression of wrinkles by applying external voltage is demonstrated. It is observed that the electric field plays a significant role in stress redistribution and guiding growth, resulting in the promotion or suppression of wrinkles, which is demonstrated by the numerical simulation of a long tubular structure. The proposed finite element scheme provides an accurate, efficient and stable tool for numerical simulation of electro-elastic solids incorporating growth effect, which can be used for understanding coupled growth phenomenon in biological soft matter and developing smart devices for medical treatment.

1. Introduction

Growth (or atrophy) phenomena of soft materials widely exist in nature and engineering, such as the growing of plant leaves and fruits, development of human organs, swelling of hydrogels and inflatable expansion of rubbers

* Corresponding authors.
E-mail addresses: c.kadapa@napier.ac.uk (C. Kadapa), Mokarram.Hossain@Swansea.ac.uk (M. Hossain), ctjwang@scut.edu.cn (J. Wang).

[1–3]. In this paper, we adopt the widely accepted viewpoint in the continuum mechanics community that the growth of soft materials can be regarded as changes in mass [1]. Due to the genetic and biochemical factors, the growth fields in soft materials are usually inhomogeneous or incompatible, which is a characteristic of the so-called differential growth. Soft materials show complex responses in the deformation process of differential growth, such as residual stresses due to incompatibility of growth fields [4], transitions of buckling modes [5], non-uniqueness of morphologies [6], stress redistributions under external loads [7] etc. The mechanism of the growth process is complicated, where mechanical, chemical, biological, and electrical factors can affect the morphological deformation of growing samples [8–11]. Although the growth mechanism of soft materials is complex, from the perspective of continuum mechanics, it is widely accepted that the growth phenomena can be regarded as variations of the component's volume or mass [1]. Generally, the growth of soft materials does not belong to the field of pure mechanics. In order to have a more comprehensive study of the growth of soft materials, some coupling models are established, such as the bio-mechanical model [11], the fluid diffusion-mechanical model [12,13], the thermo-mechanical model [14] etc. In this work, we focus on the growing electro-active material, i.e., a material having electro-mechanical responses and growth effects. Electro-active materials are popular in the area of actuators, chemical/bio-sensor electrochromic devices and artificial muscles [15–18]. A typical kind of electro-active material is electro-active polymers (EAP), which can undergo large deformation while bearing huge external force under the electric field and mechanical boundary conditions. A characteristic of a cubic EAP under a voltage difference across thickness is that contraction occurs along the thickness direction, and expansion happens in the planner directions while the volume usually remains unchanged [19,20]. EAP is one of the most promising materials for engineering applications thanks to its flexibility in generating large deformation under external electric field [21]. In addition to large voltage-induced strain, other ideal properties of dielectric elastomers include fast response, noiseless actuation, lightweight and low cost [22].

By incorporating the growth effect on electro-elastic solids, the interplay of the mechanical and the electric field will be complex and interesting. It has been demonstrated that electro-active growing materials commonly exist in the field of biology and engineering. Growth factors, intracellular signalling modulators, and feedback loops of pH and resting potential affect bioelectric states, which in turn regulate features such as stem cell differentiation and cancer cell motility [23]. The misexpression of ion-channel can cause drastic expansion of the forebrain during the embryogenesis of Xenopus laevis, leading to an abnormal electric field that influences the bioelectric signalling process between cells [24]. The external direct current electric field can change the orientation of the migration direction of the fibroblast tissue to the direction perpendicular to voltage difference [25]. Depolarization leading to a weak electrical action from tissue level is observed in Xenopus embryos during the transformation from normal cells to cancer cells [26]. Harris [27] revealed that the regional shifts of electrical potential play crucial roles in cell behaviour and tissue organization in the early development of the vertebrate limb.

In terms of applications, hydrogels with electric response are widely applied in the design of smart soft devices, and hydrogels also have growth effects such as swelling and deswelling. Coupled electromechanical growth finds straightforward applications in biology and engineering. By virtue of similarities to biological tissues and versatility in electrical, mechanical, and biofunctional engineering, some bioelectronic hydrogel devices, such as wearable and implantable devices, have been applied on human organs, e.g., brain [28], skin [29] and heart [30,31] for electrical stimulation and recording of neural activities [32]. For instance, Xu and Hayward [33] triggered the nonuniform surface pattern of a hydrogel by the external electric field, where creases formed near the anode area while the area near the cathode remained flat. By applying an electric field on the ion cross-linked hydrogel, the mechanical properties of the hydrogel can be tuned in a dynamic and flexible way [34]. Although some applications have been developed, little is known about the interplay of the different physical fields, including mechanical and electrical fields, which is a challenging task in biology and engineering.

From the theoretical modelling perspective, deformable soft materials are usually considered as hyperelastic materials. Due to the large deformation of growing soft material, the theoretical models should be proposed within the finite strain framework. To describe the growth effects on elastic solids, *volume growth theory* has been adopted in the literature to study the distribution of stress and instabilities during the growth process [35–38]. In most of the existing growth models, the total deformation gradient tensor $\boldsymbol{F}$ is decomposed into an elastic tensor $\boldsymbol{F}^e$ and a growth tensor $\boldsymbol{F}^g$, i.e, $\boldsymbol{F} = \boldsymbol{F}^e \boldsymbol{F}^g$ [39,40]. Induced by the growth tensor $\boldsymbol{F}^g$, the reference configuration reaches to a virtual intermediate configuration, where the compatibility condition $\nabla \times \boldsymbol{F}^g = \boldsymbol{0}$ is usually not satisfied due to the inhomogeneity of differential growth. The elastic deformation tensor $\boldsymbol{F}^e$ can generate residual stress on

the intermediate configuration and eventually recover the current configuration. In addition, the growth tensor is regarded as a given function of the input variable due to the fact that the growth process is much slower than the elastic response [41]. As for the modelling of electro-active materials, one needs to consider the coupling effects between mechanical and electric fields at finite strains. Governing equations of nonlinear electro-elasticity based on continuum thermomechanics are well established regarding to the nonlinear static and dynamic problems [42]. The interaction between electric fields and elastic deformation of the electro-elastic solids is investigated in [43], which is further extended to the instability analysis of electro-elastic solids through incremental theory [44,45]. The theories mentioned in [43–45] are established based on the notion of the Maxwell stress, and the governing equations are in the Lagrangian form. From a different starting point of thermodynamics, Suo et al. [46] use virtual work to derive the field equations without introducing electric force, where the stress is work conjugated to the deformation gradient, and the electric displacement is work conjugated to the electric field. Similar works of formulation derivation based on the thermodynamical framework can be found in [47–50]. To the best of the authors' knowledge, existing literature rarely considers the growth model, including both the mechanical and electrical behaviour of electro-active materials. Very recently, Du et al. [7] has adopted *volume growth theory* to describe the electro-mechanical growth phenomenon based on the framework of nonlinear electro-elastostatics [44], where the multiplicative decomposition of the deformation gradient tensor is adopted. Although some prototype problems under simple boundary conditions are investigated in [7], it is still far from the application in practical conditions where the geometry of a sample is usually complex that requires a robust numerical framework. The finite element method is a versatile mathematical tool for studying the nonlinear interplay behaviour such as the evolution of surface patterns, formation of creases or wrinkles, period-doubling etc. [51–55].

In recent years, there has been an increasing amount of literature on the finite element simulation of coupling behaviours between an electrical field and a mechanical field [56–58]. The variational formulation is built based on the basic equations in non-linear electro-elasticity in an early work of Vu et al. [59], which is further developed by Bustamante [60] and Vogel [61] using three-field formulation (displacement-pressure-Jacobian). Since electro-elastic materials are usually incompressible, they pose a serious challenge in finite element simulations. To eliminate the possible volumetric locking in the simulation of nearly incompressible materials, $\boldsymbol{F}$-bar method proposed by de Souza Neto et al. [62] is extended to the electro-elastic couple problem by Henann et al. [63]. However, the $\boldsymbol{F}$-bar method introduces a modified deformation gradient that complicates the linearization process. To improve computational efficiency, the J-bar formulation is applied to the electro-elastic couple problem by Sharma and Joglekar [56] based on a staggered algorithm for solving the coupling problem of the displacement field and electric field. Recently, a reduced mixed finite element formulation is utilized to simulate the nearly incompressible electro-viscoelastic materials [64,65], but it has limitations in tackling truly incompressible materials.

The last two decades have seen a growing trend towards finite element framework for electro-elastic materials; however, there is a lack of an accurate, robust, and computationally efficient numerical framework of the electro-elasticity incorporated with growth. The issues and limitations of widely-used finite element schemes in the computational electromechanics community are:

- To our knowledge, a numerical framework of the electro-elasticity incorporated with the growth effect is not established. Although some analytical solutions for growing electro-elastic materials are available in the literature, these analytical solutions rely on the simplicity of boundary conditions and constitutive relations. These analytical results cannot meet the requirements of capturing the non-linear responses of structures in practical cases, where the geometry, material model, and loading conditions are much more complicated.
- Both $\boldsymbol{F}$-bar and J-bar methods suffer from increasing computational cost when Poisson's ratio approaches 0.5, limiting their capability in simulating large-scale finite element models.
- The three-field formulation (displacement-pressure-Jacobian) with the Q1/P0 element [66] is effective in modelling nearly incompressible materials, and the computational efforts are significantly reduced compared with $\boldsymbol{F}$-bar and J-bar methods. However, it suffers from spurious pressure mode when Poisson's ratio approaches 0.5 due to the lack of *inf–sup* or Ladyzhenskaya–Babuska–Brezzi (LBB) stability [67,68].
- The three methods mentioned above do not apply to truly incompressible materials, which limits the accuracy of imposing the incompressibility constraint.

The objectives of this paper are: to establish a finite element framework for electro-elasticity incorporated growth effects; to use novel formulation to capture behaviours of both compressible and incompressible materials;

to implement the proposed framework through subroutine with a quadratic element that is *inf–sup* stable and computationally efficient.

In this work, we extend the finite element framework for electro-elasticity recently proposed by Kadapa and Hossain [69], to simulate electro-elasticity problems with combined growth and electric field effects. The governing equations for electro-elasto-statics problem with growth effects presented in this work are in the style of Du et al. [7]. To address the volumetric locking problem of an incompressible material, we follow the two-field mixed (displacement-pressure) formulation proposed in [70,71] when an electric potential field is omitted, which is computationally efficient and applicable for both compressible and incompressible materials. In the presence of electrical potential, we adopt a three-field formulation (displacement-pressure-potential) for capturing the nonlinearity of electro-elastic solids subjected to differential growth. Several advantages of this contribution are highlighted as:

1. To our knowledge, we will propose, for the first time, a numerical framework for the electro-elasticity incorporating growth effects. This numerical framework plays an important role in capturing the coupling behaviours of electro-elastic solids and benefiting the design of smart soft devices.
2. By adopting the two-field mixed formulation in pure mechanical cases, the proposed framework is applicable for both compressible, nearly incompressible and perfectly incompressible materials.
3. The framework overcomes the volumetric locking issue without causing extra computational burden like F-bar and J-bar methods when Poisson's ratio approaches 0.5.
4. We develop the Q2/Q1 (quadratic) 3D element to implement the numerical framework, which can capture strong non-linear behaviours in large deformation. Compared with the widely used Q1/P0 element, which is not *inf–sup* stable, the Q2/Q1 element is not only *inf–sup* stable but also computationally efficient in capturing extremely large deformations.
5. The numerical framework is implemented through a user element subroutine (UEL) in ABAQUS, offering pre-and post-processing.

This paper is organized as follows: Section 2 introduces the governing equations for nonlinear electromechanics incorporated with the growth effect. Modifications for incompressible materials and material models are also introduced in Section 2 as a prelude to establishing a finite element framework. In Section 3, we propose the finite element formulation used in this work. Some numerical examples are given in Section 4 to illustrate the accuracy and efficiency of the proposed FEM framework. Conclusions and outlook for the future are summarized in Section 5.

2. Governing equations for nonlinear electromechanics with growth effects

2.1. Kinematics, strain and stress

Consider a homogeneous electro-elastic solid body with the reference configuration $\mathcal{B}_r$ in the 3D Euclidean space R^3. The solid body is subjected to external forces or electrical stimuli or internal stresses induced by the growth or a combination of all, and it reaches the current configuration $\mathcal{B}_t$. The position vector in the reference and the current configurations is denoted by X and x, respectively. The displacement field is defined as

$$u(X) = x(X) - X. \tag{1}$$

Then, based on the definition in (1), the total deformation gradient tensor F, and its determinant J are given as

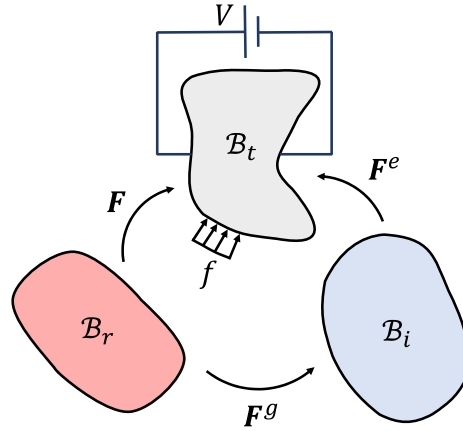$$F = \frac{\partial x}{\partial X} = I + \frac{\partial u}{\partial X}, \quad \text{and} \quad J = \det F, \tag{2}$$

where I is a second order identity tensor. Following the classical assumption of growth mechanics [35,39,40], the total deformation gradient tensor is decomposed multiplicatively into an elastic part F^e, and a growth part F^g, as

$$F = F^e F^g. \tag{3}$$

Using the decomposition of F in (3), the determinant J can be written as

$$J = J^e J^g, \tag{4}$$

Fig. 1. Kinematics: the total deformation can be decomposed into growth and elastic deformations.

where,

$$J^e = \det \boldsymbol{F}^e, \quad \text{and} \quad J^g = \det \boldsymbol{F}^g. \tag{5}$$

In this work, the growth tensor $\boldsymbol{F}^g$ is assumed to be the function of the reference coordinate $\boldsymbol{X}$ only, without considering the coupling effect with mechanical load and electrical stimuli. As shown in Fig. 1 the deformation of the solid body can be decomposed into two steps; the first step is the deformation from the reference configuration $\mathcal{B}_r$ to an intermediate stress-free configuration $\mathcal{B}_i$ under pure growth, and the second step is from the intermediate configuration $\mathcal{B}_i$ to current configuration $\mathcal{B}_t$ with growth and elastic response.

The grown configuration $\mathcal{B}_i$ is determined by $\boldsymbol{F}^g$, where the compatibility condition $\nabla \times \boldsymbol{F}^g = \boldsymbol{0}$ may not be satisfied, resulting in discontinuity and overlapping. In the current configuration $\mathcal{B}_t$, residual stresses are triggered by the incompatibility of the growth field, mechanical boundary condition, as well as electrical stimuli.

For soft materials (e.g., soft biological tissues, polymeric gels), the elastic deformations are usually isochoric so that

$$\mathcal{R}(\boldsymbol{F}^e, \boldsymbol{F}^g) = J^g \mathcal{R}_0(\boldsymbol{F}^e) = J^g \left(\det \boldsymbol{F}^e - 1 \right) = 0, \tag{6}$$

This incompressibility constraint ensures that the pure elastic deformation of material does not result in a change in the volume.

For modelling truly incompressible hyperelastic materials in the finite strain regime, the elastic part of the deformation gradient $\boldsymbol{F}^e$ is decomposed into volumetric and deviatoric components (refer to Ogden [72] and Bonet and Wood [73] for the details) as

$$\boldsymbol{F}^e = \boldsymbol{F}^e_{\text{vol}} \boldsymbol{F}^e_{\text{dev}}, \tag{7}$$

where

$$\boldsymbol{F}^e_{\text{vol}} = J^{e^{1/3}} \boldsymbol{I}, \quad \boldsymbol{F}^e_{\text{dev}} = J^{e^{-1/3}} \boldsymbol{F}^e. \tag{8}$$

Using the above definitions, the modified elastic deformation gradient tensor and the right Cauchy–Green tensor are defined as

$$\text{Modified elastic deformation gradient,} \quad \overline{\boldsymbol{F}}^e := J^{e^{-1/3}} \boldsymbol{F}^e \tag{9}$$

$$\text{Modified right Cauchy–Green deformation tensor,} \quad \overline{\boldsymbol{C}}^e := \overline{\boldsymbol{F}}^{e\text{T}} \overline{\boldsymbol{F}}^e. \tag{10}$$

The other quantities are modified accordingly [69]. It is worth mentioning that the modified quantities are with respect to the virtual stress-free configuration $\mathcal{B}_i$.

Remarks. The mechanisms of growth phenomena in soft materials are complex, in which growth fields can be generated by internal factors such as gene and cell division, or external factors such as infusion or evaporation of

Table 1
Electric field quantities in different configurations.

Configuration	Reference ($\mathcal{B}_r$)	Intermediate ($\mathcal{B}_i$)	Current ($\mathcal{B}_t$)
Electric field vector	$\mathbb{E}$	$\bar{\mathbb{E}}$	$\mathbb{e}$
Electric displacement vector	$\mathbb{D}$	$\bar{\mathbb{D}}$	$\mathbb{d}$

water, temperature and pressure. Due to the complexity of the mechanisms of growth, the growth fields in the soft material samples are usually inhomogeneous or incompatible. To describe the growth effect of soft materials, the growth tensor $\boldsymbol{F}^g$ is chosen to be a symmetric second order tensor [37], such that it can be used to describe the inherent inhomogeneity and incompatibility of growth fields in soft material samples.

2.2. Electrostatics

To describe electrostatics, we introduce Faraday's and Gauss's laws. Since the elastic strains are triggered during the deformation from $\mathcal{B}_i$ to $\mathcal{B}_t$, the energy function Ψ is defined in the virtual stress-free grown configuration $\mathcal{B}_i$. Here, the two quantities corresponding to the electric field in three different configurations are listed in Table 1.

These quantities in different configurations are related by the pull-back operation as given by

$$\mathbb{E} = \boldsymbol{F}^{\mathrm{T}}\mathbb{e} = \boldsymbol{F}^{g^{\mathrm{T}}}\bar{\mathbb{E}}, \tag{11}$$

$$\mathbb{D} = J\boldsymbol{F}^{-1}\mathbb{d} = J^g\boldsymbol{F}^{g^{-1}}\bar{\mathbb{D}}, \tag{12}$$

where

$$\bar{\mathbb{E}} = \boldsymbol{F}^{e^{\mathrm{T}}}\mathbb{e}, \tag{13}$$

$$\bar{\mathbb{D}} = J^e\boldsymbol{F}^{e^{-1}}\mathbb{d}. \tag{14}$$

In the absence of free charges and currents, Faraday's and Gauss's laws can be expressed using the electrical quantities listed in Table 1, as

$$\begin{aligned}\operatorname{curl}\mathbb{e} &= \nabla_{\boldsymbol{x}} \times \mathbb{e} = \boldsymbol{0}, \\ \operatorname{div}\mathbb{d} &= \nabla_{\boldsymbol{x}} \cdot \mathbb{d} = 0,\end{aligned} \tag{15}$$

where $\nabla_{\boldsymbol{x}}$ is the gradient operator with respect to the current configuration. Since $\operatorname{curl}\mathbb{e} = \boldsymbol{0}$, there exists a twice continuously differentiable scalar electric field ϕ such that

$$\mathbb{e} = -\nabla_{\boldsymbol{x}}\phi. \tag{16}$$

Eq. (16) automatically satisfies Faraday's law (15)$_1$.

The complete set of governing equations for the electro-mechanical growth problem in the current configuration can be written as

$$\begin{aligned}-\nabla_{\boldsymbol{x}} \cdot \boldsymbol{\sigma} &= \boldsymbol{f} & \forall \boldsymbol{x} \in \mathcal{B}_t \tag{17a}\\ \nabla_{\boldsymbol{x}} \cdot \mathbb{d} &= 0 & \forall \boldsymbol{x} \in \mathcal{B}_t \tag{17b}\\ \boldsymbol{u}(\boldsymbol{x}) &= \bar{\boldsymbol{u}}(\boldsymbol{x}) & \forall \boldsymbol{x} \in \partial\mathcal{B}_t^{\mathrm{mech,D}} \tag{17c}\\ \boldsymbol{\sigma}(\boldsymbol{x}) \cdot \boldsymbol{n} &= \bar{\boldsymbol{t}}(\boldsymbol{x}) & \forall \boldsymbol{x} \in \partial\mathcal{B}_t^{\mathrm{mech,N}} \tag{17d}\\ \phi(\boldsymbol{x}) &= \bar{\phi}(\boldsymbol{x}) & \forall \boldsymbol{x} \in \partial\mathcal{B}_t^{\mathrm{elec,D}} \tag{17e}\\ -\mathbb{d}(\boldsymbol{x}) \cdot \boldsymbol{n} &= \bar{\omega}(\boldsymbol{x}) & \forall \boldsymbol{x} \in \partial\mathcal{B}_t^{\mathrm{elec,N}} \tag{17f}\end{aligned}$$

where $\boldsymbol{\sigma}$ is the Cauchy stress, $\boldsymbol{f}$ is the body force per unit deformed volume, $\boldsymbol{n}$ is the unit outward normal on the boundary $\partial\mathcal{B}_t$, $\bar{\boldsymbol{u}}(\boldsymbol{x})$ is the prescribed value of displacement on the Dirichlet boundary $\mathcal{B}_t^{\mathrm{mech,D}}$, $\bar{\boldsymbol{t}}(\boldsymbol{x})$ is the specified traction force per unit deformed area on the Neumann boundary $\mathcal{B}_t^{\mathrm{mech,N}}$, $\bar{\phi}(\boldsymbol{x})$ is the prescribed value of electric potential on the Dirichlet boundary $\mathcal{B}_t^{\mathrm{elec,D}}$, $\bar{\omega}(\boldsymbol{x})$ is the specified electric surface charge density per unit deformed area on the Neumann boundary $\mathcal{B}_t^{\mathrm{elec,N}}$.

2.3. Constitutive models and stress–strain relations

Since the virtual configuration is stress-free, elastic strains are generated during the deformation from $\mathcal{B}_i$ to $\mathcal{B}_t$, resulting from the mechanical load and electrical stimuli. Thus, the strain energy function is a function of elastic deformation gradient $\bar{\boldsymbol{F}}^e$ and electric field vector $\bar{\mathbb{E}}$. Generally, the strain energy function for the hyperelastic materials is assumed to be decomposed into a deviatoric part $\Psi^{\mathrm{mech,dev}}$, a volumetric part $\Psi^{\mathrm{mech,vol}}$, and an electric-mechanical coupled part Ψ^{coup} as

$$\Psi(\bar{\boldsymbol{F}}^e, \bar{\mathbb{E}}) = \Psi^{\mathrm{mech,dev}}(\bar{\boldsymbol{F}}^e) + \Psi^{\mathrm{mech,vol}}(J^e) + \Psi^{\mathrm{coup}}(\boldsymbol{F}^e, \bar{\mathbb{E}}). \tag{18}$$

For nearly incompressible material, several expressions for volumetric energy function $\Psi^{\mathrm{mech,vol}}$ have been adopted to describe material behaviour (see [71] for details). In the case of a perfectly incompressible material, the volumetric energy function $\Psi^{\mathrm{mech,vol}}$ vanishes. To capture the behaviour of perfectly incompressible material, the strain energy function adopted in the following content of this paper is given as

$$\Psi(\bar{\boldsymbol{F}}^e, \bar{\mathbb{E}}) = \Psi^{\mathrm{mech,dev}}(\bar{\boldsymbol{F}}^e) + \Psi^{\mathrm{coup}}(\boldsymbol{F}^e, \bar{\mathbb{E}}). \tag{19}$$

The effective first Piola–Kirchhoff stress for the mixed formulation is defined as

$$\hat{\boldsymbol{P}} := \frac{\partial(\Psi^{\mathrm{mech,dev}} + \Psi^{\mathrm{coup}})}{\partial \boldsymbol{F}} + pJ^e \boldsymbol{F}^{e^{-\mathrm{T}}} = \bar{\boldsymbol{P}} + pJ^e \boldsymbol{F}^{e^{-\mathrm{T}}}, \tag{20}$$

where p is an arbitrary Lagrange multiplier accounting for the hydrostatic pressure. The effective Cauchy stress for the mixed formulation is defined as

$$\hat{\boldsymbol{\sigma}} := \frac{1}{J^e}\hat{\boldsymbol{P}}\boldsymbol{F}^{e^{\mathrm{T}}} = \frac{1}{J^e}\bar{\boldsymbol{P}}\boldsymbol{F}^{e^{\mathrm{T}}} + p\boldsymbol{I}. \tag{21}$$

Since the total deformation consists of growth and elastic deformation, the derivative with respect to the deformation gradient $\boldsymbol{F}$ is calculated using the chain rule. $\bar{\boldsymbol{P}}$ is given by the first derivative of $\Psi(\bar{\boldsymbol{F}}^e, \bar{\mathbb{E}})$ with respect to $\boldsymbol{F}$

$$\begin{aligned}\bar{P}_{iJ} &= \frac{\partial(\Psi^{\mathrm{mech,dev}} + \Psi^{\mathrm{coup}})}{\partial F_{iJ}} = \frac{\partial(\Psi^{\mathrm{mech,dev}} + \Psi^{\mathrm{coup}})}{\partial F_{iM}^e}\frac{\partial F_{iM}^e}{\partial F_{iJ}} \\ &= \frac{\partial(\Psi^{\mathrm{mech,dev}} + \Psi^{\mathrm{coup}})}{\partial F_{iM}^e}\frac{\partial F_{iN}F_{NM}^{g^{-1}}}{\partial F_{iJ}} = \bar{P}_{iM}^e F_{JM}^{g^{-1}},\end{aligned} \tag{22}$$

where $\bar{P}_{iM}^e = \partial(\Psi^{\mathrm{mech,dev}} + \Psi^{\mathrm{coup}})/\partial F_{iM}^e$. The second derivative of $\Psi(\bar{\boldsymbol{F}}^e, \bar{\mathbb{E}})$ with respect to $\boldsymbol{F}$ is given by

$$\frac{\partial^2(\Psi^{\mathrm{mech,dev}} + \Psi^{\mathrm{coup}})}{\partial F_{iJ}\partial F_{kL}} = \frac{\partial \bar{P}_{iJ}}{\partial F_{kL}} = \frac{\partial \bar{P}_{iM}^e}{\partial F_{kL}}F_{JM}^{g^{-1}} = \frac{\partial \bar{P}_{iM}^e}{\partial F_{kN}^e}F_{LN}^{g^{-1}}F_{JM}^{g^{-1}} \tag{23}$$

The first derivative of $\bar{\mathbb{D}}$ with respect to $\boldsymbol{F}$ is given by

$$\frac{\partial \bar{D}_I}{\partial F_{jK}} = \frac{\partial \bar{D}_I}{\partial F_{jM}^e}\frac{\partial F_{jM}^e}{\partial F_{jK}} = \frac{\partial \bar{D}_I}{\partial F_{jM}^e}\frac{\partial F_{jN}F_{NM}^{g^{-1}}}{\partial F_{jK}} = \frac{\partial \bar{D}_I}{\partial F_{jM}^e}F_{KM}^{g^{-1}} \tag{24}$$

From a variety of deviatoric energy functions available in the literature for modelling rubber-like materials, we have selected the energy function for Neo-Hookean material for simplicity without loosing the generality of our numerical scheme. Its energy functions is

$$\Psi^{\mathrm{mech,dev}} = \frac{\mu}{2}\left(I_{\bar{C}} - 3\right) \tag{25}$$

Furthermore, the part of the strain energy function corresponding to the electromechanical coupling is taken as the ideal electro-elastic solid [44,45]

$$\Psi^{\mathrm{coup}} = -\frac{1}{2}\epsilon J^e \boldsymbol{C}^{e^{-1}} : (\bar{\mathbb{E}} \otimes \bar{\mathbb{E}}) = -\frac{1}{2}\epsilon J^e \bar{\mathbb{E}}_I C_{IJ}^{e^{-1}} \bar{\mathbb{E}}_J, \tag{26}$$

where $\boldsymbol{C}^e = \boldsymbol{F}^{e^{\mathrm{T}}}\boldsymbol{F}^e$, $\epsilon = \epsilon_r \epsilon_0$ is the permittivity of the material and ϵ_r is the relative permittivity, also known as the dielectric constant and ϵ_0 is the vacuum permittivity. Note that the material model introduced in this work is for

the purpose of presentation. It does not mean the proposed numerical framework only applies to material models introduced above. For example, we can use the Gent and Arruda–Boyce models for the deviatoric energy functions and other kinds of electro-elastic solid model [69].

3. Finite element formulation

In order to accurately model the incompressible nature of deformations in electromechanical growth problems, we adapt the mixed displacement-pressure-potential formulation in this work. For a detailed discussion of the advantages of mixed formulations over $\boldsymbol{F}$-bar and other similar formulations, we refer the reader to Kadapa and Hossain [71] in which the mixed formulation was first proposed for the pure electromechanics problem. Since we are only interested in the incompressible or quasi-incompressible deformations in this work, we adapted the perturbed Lagrangian form as used in [71] instead of the generalized mixed formulation used for computational growth [74]. The important details of the mixed formulation for electromechanics with appropriate changes accounting for the growth effects are presented below.

The total energy functional of the electromechanical growth problem is given as

$$\Pi = \int_{\mathcal{B}_r} \left(\Psi^{\text{mech,dev}} + \Psi^{\text{coup}} + \Psi_{\text{PL}} \right) J^g \ dV - \Pi_{\text{ext}} \tag{27}$$

where dV is the elemental volume in the reference configuration. Since the integration is respect to the reference configuration $\mathcal{B}_r$ and the strain energy functions are functions of only the elastic part of total deformation, the strain energy functions are multiplied by J^g to account for the total volume change from the reference configuration to the current configuration. Ψ_{PL} is the function for imposing the incompressibility constraint (6) using the perturbed Lagrangian method. Ψ_{PL} is defined as

$$\Psi_{\text{PL}} = p(J^e - 1) - \frac{p^2}{2\kappa} \tag{28}$$

where κ is the bulk modulus of the material. For the truly incompressible case, i.e., when Poisson's ratio (ν) is 0.5, or $\kappa = \infty$, the term $p^2/(2\kappa)$ vanishes. The energy contribution due to the external forces, Π_{ext}, is given as

$$\Pi_{\text{ext}} = \int_{\mathcal{B}_r} \boldsymbol{u}^{\text{T}} \boldsymbol{f}_0 J^g \ dV + \int_{\partial \mathcal{B}_r^{\text{mech ,N}}} \boldsymbol{u}^{\text{T}} \boldsymbol{t}_0 A^g \ dA + \int_{\partial \mathcal{B}_r^{\text{elec,N}}} \phi \bar{\omega} A^g \ dA, \tag{29}$$

where A^g is the surface Jacobian due to growth, dA is the elemental area in the reference configuration, f_0 is the body force per unit original volume, $\boldsymbol{t}_0$ is the traction force per unit undeformed area, and ω_0 is the electric surface charge density per unit original area.

3.1. Variational formulations

After taking first variation of the total energy functional Π and then appropriate simplifications (see Appendix A for the details), we get

$$\delta \Pi = \int_{\mathcal{B}_r} \left(\delta u_{i,j} \hat{\sigma}_{ij} + \delta \phi_{,i} \mathrm{d}_i \right) J \ dV + \int_{\mathcal{B}_r} \delta p \left(J - J^g - \frac{p}{\kappa} J^g \right) \ dV - \delta \Pi_{\text{ext}}. \tag{30}$$

For the finite element discretization, we take the approximations for displacement ($\boldsymbol{u}$), pressure (p) and electric potential (ϕ) as

$$\boldsymbol{u} = \mathbf{N}_{\boldsymbol{u}} \mathbf{u}, \quad p = \mathbf{N}_p \mathbf{p}, \quad \text{and} \quad \phi = \mathbf{N}_\phi \boldsymbol{\phi},$$

where $\mathbf{u}$, $\mathbf{p}$ and $\boldsymbol{\phi}$ are the displacement, pressure and electric potential degrees of freedom (DOFs) defined at nodes. $\mathbf{N}_{\boldsymbol{u}}$, $\mathbf{N}_p$ and $\mathbf{N}_\phi$ are element-wise basis functions for displacement, pressure, and electric potential, respectively, which are given by

$$\mathbf{N}_{\boldsymbol{u}} = \begin{bmatrix} {}^1N_u & 0 & 0 & \dots & {}^{\text{nu}}N_u & 0 & 0 \\ 0 & {}^1N_u & 0 & \dots & 0 & {}^{\text{nu}}N_u & 0 \\ 0 & 0 & {}^1N_u & \dots & 0 & 0 & {}^{\text{nu}}N_u \end{bmatrix}$$

$$\mathbf{N}_p = \begin{bmatrix} {}^1N_p & {}^2N_p & \dots & {}^{\text{np}}N_p \end{bmatrix}$$

$$\mathbf{N}_\phi = \begin{bmatrix} {}^1 N_\phi & {}^2 N_\phi & \cdots & {}^{n\phi} N_\phi \end{bmatrix}$$

where nu, np and $n\phi$ are the number of the corresponding basis functions. With these approximations, the first variations of the solution variables become

$$\delta \boldsymbol{u} = \mathbf{N}_{\boldsymbol{u}}\, \delta\mathbf{u}, \quad \delta p = \mathbf{N}_p\, \delta\mathbf{p}, \quad \text{and} \quad \delta\phi = \mathbf{N}_\phi\, \delta\boldsymbol{\phi}. \tag{31}$$

The gradient of the displacement field is represented as

$$\begin{aligned}
\nabla_x \boldsymbol{u} = u_{i,j} &= \begin{bmatrix} u_{x,x} & u_{y,x} & u_{z,x} & u_{x,y} & u_{y,y} & u_{z,y} & u_{x,z} & u_{y,z} & u_{z,z} \end{bmatrix}^{\mathrm{T}} \\
&= \begin{bmatrix} \frac{\partial u_x}{\partial x} & \frac{\partial u_y}{\partial x} & \frac{\partial u_z}{\partial x} & \frac{\partial u_x}{\partial y} & \frac{\partial u_y}{\partial y} & \frac{\partial u_z}{\partial y} & \frac{\partial u_x}{\partial z} & \frac{\partial u_y}{\partial z} & \frac{\partial u_z}{\partial z} \end{bmatrix}^{\mathrm{T}} \\
&= \mathbf{G}_{\boldsymbol{u}}\mathbf{u}
\end{aligned} \tag{32}$$

where $\mathbf{G}_{\boldsymbol{u}}$ is the gradient-displacement matrix which, for a single basis function, is given as

$$\mathbf{G}_{\boldsymbol{u}} = \begin{bmatrix} \frac{\partial N_{\boldsymbol{u}}}{\partial x} & 0 & 0 & \frac{\partial N_{\boldsymbol{u}}}{\partial y} & 0 & 0 & \frac{\partial N_{\boldsymbol{u}}}{\partial z} & 0 & 0 \\ 0 & \frac{\partial N_{\boldsymbol{u}}}{\partial x} & 0 & 0 & \frac{\partial N_{\boldsymbol{u}}}{\partial y} & 0 & 0 & \frac{\partial N_{\boldsymbol{u}}}{\partial z} & 0 \\ 0 & 0 & \frac{\partial N_{\boldsymbol{u}}}{\partial x} & 0 & 0 & \frac{\partial N_{\boldsymbol{u}}}{\partial y} & 0 & 0 & \frac{\partial N_{\boldsymbol{u}}}{\partial z} \end{bmatrix}^{\mathrm{T}} \tag{33}$$

Similarly, the gradient of the electric potential in the current configuration is computed as

$$\nabla_x \phi = \phi_{,i} = \begin{bmatrix} \frac{\partial \phi}{\partial x} & \frac{\partial \phi}{\partial y} & \frac{\partial \phi}{\partial z} \end{bmatrix}^{\mathrm{T}} = \mathbf{G}_\phi \boldsymbol{\phi}, \tag{34}$$

where the gradient-potential matrix $\mathbf{G}_\phi$ for a single basis function is

$$\mathbf{G}_\phi = \begin{bmatrix} \frac{\partial N_\phi}{\partial x} & \frac{\partial N_\phi}{\partial y} & \frac{\partial N_\phi}{\partial z} \end{bmatrix}^{\mathrm{T}}. \tag{35}$$

For the derivation of stiffness matrices in this work, we introduce a divergence-displacement matrix, $\mathbf{D}_u$, for representing the divergence of the displacement in the vector form as

$$\nabla_x \cdot \boldsymbol{u} = u_{i,i} = \frac{\partial u_x}{\partial x} + \frac{\partial u_y}{\partial y} + \frac{\partial u_z}{\partial z} = \mathbf{D}_u \mathbf{u} \tag{36}$$

with $\mathbf{D}_u$ for a single basis function as given by

$$\mathbf{D}_u = \begin{bmatrix} \frac{\partial N_u}{\partial x} & \frac{\partial N_u}{\partial y} & \frac{\partial N_u}{\partial z} \end{bmatrix}. \tag{37}$$

For the ease of computer implementation of the finite element formulation, the effective Cauchy stress tensor is written as a column vector as

$$\begin{aligned}
\hat{\boldsymbol{\sigma}} = \hat{\sigma}_{ij} &= \begin{bmatrix} \hat{\sigma}_{xx} & \hat{\sigma}_{yx} & \hat{\sigma}_{zx} & \hat{\sigma}_{xy} & \hat{\sigma}_{yy} & \hat{\sigma}_{zy} & \hat{\sigma}_{xz} & \hat{\sigma}_{yz} & \hat{\sigma}_{zz} \end{bmatrix}^{\mathrm{T}} \\
&= \begin{bmatrix} \hat{\sigma}_{11} & \hat{\sigma}_{21} & \hat{\sigma}_{31} & \hat{\sigma}_{12} & \hat{\sigma}_{22} & \hat{\sigma}_{32} & \hat{\sigma}_{13} & \hat{\sigma}_{23} & \hat{\sigma}_{33} \end{bmatrix}^{\mathrm{T}}.
\end{aligned} \tag{38}$$

By substituting the first variations of the field variables (31) into the first variation of Π given in (30), the resulting semi-discrete equations for the electromechanical growth problem with mixed formulation can be written as

$$\begin{aligned}
\mathbf{R}_u &= \mathbf{F}_{\boldsymbol{u}}^{\mathrm{int}} - \mathbf{F}_{\boldsymbol{u}}^{\mathrm{ext}} = \mathbf{0}, \\
\mathbf{R}_\phi &= \mathbf{F}_\phi^{\mathrm{int}} - \mathbf{F}_\phi^{\mathrm{ext}} = \mathbf{0}, \\
\mathbf{R}_p &= \mathbf{F}_p^{\mathrm{int}} = \mathbf{0},
\end{aligned} \tag{39}$$

where $\mathbf{F}_{\boldsymbol{u}}^{\mathrm{int}}$, $\mathbf{F}_p^{\mathrm{int}}$ and $\mathbf{F}_\phi^{\mathrm{int}}$ are the vectors of internal forces for the displacement, pressure and potential fields, respectively. $\mathbf{F}_{\boldsymbol{u}}^{\mathrm{ext}}$ and $\mathbf{F}_\phi^{\mathrm{ext}}$ are the vectors of external forces for the displacement and potential fields. Based on

(29) and (30), these internal and external force vectors are given by

$$\mathbf{F}_{\boldsymbol{u}}^{\text{int}} = \int_{\mathcal{B}_t} \mathbf{G}_{\boldsymbol{u}}^{\text{T}} \hat{\boldsymbol{\sigma}} \ \mathrm{d}v,$$

$$\mathbf{F}_{p}^{\text{int}} = \int_{\mathcal{B}_r} \mathbf{N}_{p}^{\text{T}} \left(J - J^g - \frac{p}{\kappa} J^g \right) \ \mathrm{d}V,$$

$$\mathbf{F}_{\phi}^{\text{int}} = \int_{\mathcal{B}_t} \mathbf{G}_{\phi}^{\text{T}} \mathrm{d} \ \mathrm{d}v, \tag{40}$$

$$\mathbf{F}_{\boldsymbol{u}}^{\text{ext}} = \int_{\mathcal{B}_r} \mathbf{N}_{\boldsymbol{u}}^{\text{T}} \boldsymbol{f}_0 J^g \ \mathrm{d}V + \int_{\partial \mathcal{B}_r^{\text{mech},\text{N}}} \mathbf{N}_{\boldsymbol{u}}^{\text{T}} \boldsymbol{t}_0 A^g \ \mathrm{d}A,$$

$$\mathbf{F}_{\phi}^{\text{ext}} = \int_{\partial \mathcal{B}_r^{\text{elec, N}}} \mathbf{N}_{\phi} \omega_0 A^g \ \mathrm{d}A,$$

where $\mathrm{d}v = J \mathrm{d}V$ is the elemental volume in the current configuration.

3.2. Newton–Raphson scheme

The coupled nonlinear equations (39) are solved using an incremental iterative approach. The subscripts n and $n + 1$ denote for the previously converged load step and current load step, respectively. Then the displacement, electric potential, pressure DOFs (degrees of freedom) and growth tensor at the nth converged load step are $\mathbf{u}_n$, $\boldsymbol{\phi}_n$, $\mathbf{p}_n$ and $\boldsymbol{F}_n^g$, respectively. The corresponding DOFs at the current load step are computed as

$$\mathbf{u}_{n+1} = \mathbf{u}_n + \Delta \mathbf{u},$$

$$\boldsymbol{\phi}_{n+1} = \boldsymbol{\phi}_n + \Delta \boldsymbol{\phi},$$

$$\mathbf{p}_{n+1} = \mathbf{p}_n + \Delta \mathbf{p}, \tag{41}$$

$$\boldsymbol{F}_{n+1}^g = \boldsymbol{F}_n^g + \Delta \boldsymbol{F}^g,$$

where $\Delta \mathbf{u}$, $\Delta \boldsymbol{\phi}$, $\Delta \mathbf{p}$ and $\Delta \boldsymbol{F}^g$ are the load step increments from step n to $n+1$. Here, the increment of growth tensor $\Delta \boldsymbol{F}^g$ is considered as an input variable. By adopting the Newton–Raphson scheme, solution variables involved in the coupled nonlinear equations (39) are solved at every load step iteratively. The subscripts k and $k + 1$ denote previous and current iterations, respectively. Assuming the iterative increments of displacement, electric potential and pressure fields are $\bar{\Delta} \mathbf{u}$, $\bar{\Delta} \boldsymbol{\phi}$ and $\bar{\Delta} \mathbf{p}$, respectively, the respective quantities at the current iteration can be written as

$$\mathbf{u}_{n+1}^{(k+1)} = \mathbf{u}_n + \Delta \mathbf{u}^{(k+1)} = \mathbf{u}_n + \Delta \mathbf{u}^{(k)} + \bar{\Delta} \mathbf{u} = \mathbf{u}_{n+1}^{(k)} + \bar{\Delta} \mathbf{u},$$

$$\boldsymbol{\phi}_{n+1}^{(k+1)} = \boldsymbol{\phi}_n + \Delta \boldsymbol{\phi}^{(k+1)} = \boldsymbol{\phi}_n + \Delta \boldsymbol{\phi}^{(k)} + \bar{\Delta} \boldsymbol{\phi} = \boldsymbol{\phi}_{n+1}^{(k)} + \bar{\Delta} \boldsymbol{\phi}, \tag{42}$$

$$\mathbf{p}_{n+1}^{(k+1)} = \mathbf{p}_n + \Delta \mathbf{p}^{(k+1)} = \mathbf{p}_n + \Delta \mathbf{p}^{(k)} + \bar{\Delta} \mathbf{p} = \mathbf{p}_{n+1}^{(k)} + \bar{\Delta} \mathbf{p},$$

where k can run from 1 to $k_{\max}$, the maximum number of iterations.

In order to solve the coupled nonlinear equations (39) using the Newton–Raphson scheme, we need to linearize $\delta \Pi$. By taking the second variation $d(\cdot)$ of Π, we get

$$d(\delta \Pi) = \int_{\mathcal{B}_r} \left(\delta u_{i,j} \mathrm{e}_{ijkl} J du_{k,l} - \delta u_{i,j} \mathrm{p}_{ijk} J d\phi_{,k} + \delta \phi_{,i} \hat{\mathrm{p}}_{ijl} J du_{j,l} - \delta \phi_{,i} \mathrm{d}_{ik} J d\phi_{,k} \right.$$

$$\left. + \delta p J du_{i,i} - \delta p \frac{J^g}{\kappa} dp + \delta u_{k,k} J dp \right) \ \mathrm{d}V, \tag{43}$$

where e_{ijkl} is the material tangent tensor of order four; p_{ijk} and $\hat{\mathrm{p}}_{ijl}$ are third-order coupling tensors; and d_{ik} is the electric permittivity tensor of order two, and they are given in Appendix B.

By substituting the corresponding finite element approximations in (43), we obtain the following discrete matrix system for the incremental displacements, $\bar{\Delta} \boldsymbol{u}$, incremental pressure, $\bar{\Delta} p$, and incremental electric potential, $\bar{\Delta} \phi$, at iteration $k + 1$,

$$\begin{bmatrix} \mathbf{K}_{\boldsymbol{uu}} & \mathbf{K}_{\boldsymbol{u\phi}} & \mathbf{K}_{\boldsymbol{u}p} \\ \mathbf{K}_{\boldsymbol{\phi u}} & \mathbf{K}_{\boldsymbol{\phi\phi}} & \mathbf{0} \\ \mathbf{K}_{p\boldsymbol{u}} & \mathbf{0} & \mathbf{K}_{pp} \end{bmatrix} \begin{Bmatrix} \bar{\Delta} \mathbf{u} \\ \bar{\Delta} \boldsymbol{\phi} \\ \bar{\Delta} \mathbf{p} \end{Bmatrix} = - \begin{Bmatrix} \mathbf{R}_{\boldsymbol{u}} \\ \mathbf{R}_{\phi} \\ \mathbf{R}_p \end{Bmatrix}, \tag{44}$$
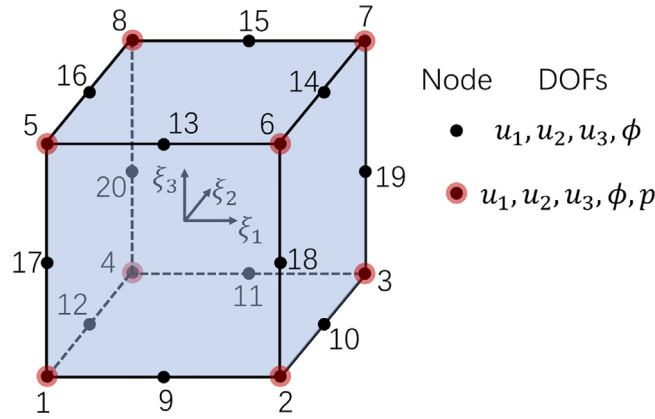
Fig. 2. The 20-noded hexahedral element with different DOFs.

where

$$\mathbf{K}_{uu} = \int_{\mathcal{B}_t} \mathbf{G}_u^{\mathrm{T}} \mathbf{e} \mathbf{G}_u \ \mathrm{d}v,$$

$$\mathbf{K}_{up} = \int_{\mathcal{B}_t} \mathbf{D}_u^{\mathrm{T}} \mathbf{N}_p \ \mathrm{d}v = \mathbf{K}_{pu}^{\mathrm{T}},$$

$$\mathbf{K}_{u\phi} = -\int_{\mathcal{B}_t} \mathbf{G}_u^{\mathrm{T}} \mathbf{p} \mathbf{G}_\phi \mathrm{d}v = \mathbf{K}_{\phi u}^{\mathrm{T}}, \tag{45}$$

$$\mathbf{K}_{pp} = -\int_{\mathcal{B}_r} \frac{1}{\kappa} \mathbf{N}_p^{\mathrm{T}} \mathbf{N}_p \ \mathrm{d}V,$$

$$\mathbf{K}_{\phi\phi} = -\int_{\mathcal{B}_t} \mathbf{G}_\phi^{\mathrm{T}} \mathbf{d} \mathbf{G}_\phi \mathrm{d}v.$$

3.3. Finite element spaces

Following the advantages of the higher-order elements for soft incompressible materials demonstrated in our previous work [69,74], we adapt a second-order element in this work. As shown in Fig. 2, we use a 20-node hexahedral element (C3D20) for the displacement and electric potential fields and 8-node hexahedral element for the pressure field. The element combination for displacement/pressure/electric potential field is denoted as Q2/Q1/Q2.

Remarks. Since the approximation for the electric field is not linked to the LBB condition, we can use linear or quadratic or further higher-order approximation for the electric field, independent of that of displacement. To achieve higher accuracy per node or element, a quadratic approximation for the electric field is adopted. In addition, the Cauchy stress is a function of the first derivative of displacement, pressure, and the first derivative of electric potential. The quadratic approximation for the electric field can also enhance the accuracy of the total stress calculated at quadrature points.

The finite element formulation for electromechanical growth is implemented a user-defined element subroutine (UEL) in FEA software ABAQUS. UEL subroutine is suitable for modelling multi-physical processes that are coupled to structural behaviour. In a UEL subroutine, a user can define element order, basis functions and material tangent stiffness, so it can realize elements and materials of different complexity. The nodes on the isoparametric element are numbered following ABAQUS's conventions, in which the DOFs for nodes 1–8 are displacement, electric potential and pressure, while for nodes 9–20, the DOFs are displacement and electric potential, as shown in Fig. 2. With 20×3 displacement DOFs, 20 electric potential DOFs and 8 pressure DOFs, there are 88 DOFs in total per each element. So the dimension of element stiffness is 88×88.

In the beginning of the iteration, UEL is called to calculate the element stiffness matrix and residual force vector, i.e., to define the contribution of the element to the model. A flowchart of UEL is shown in Fig. 3.
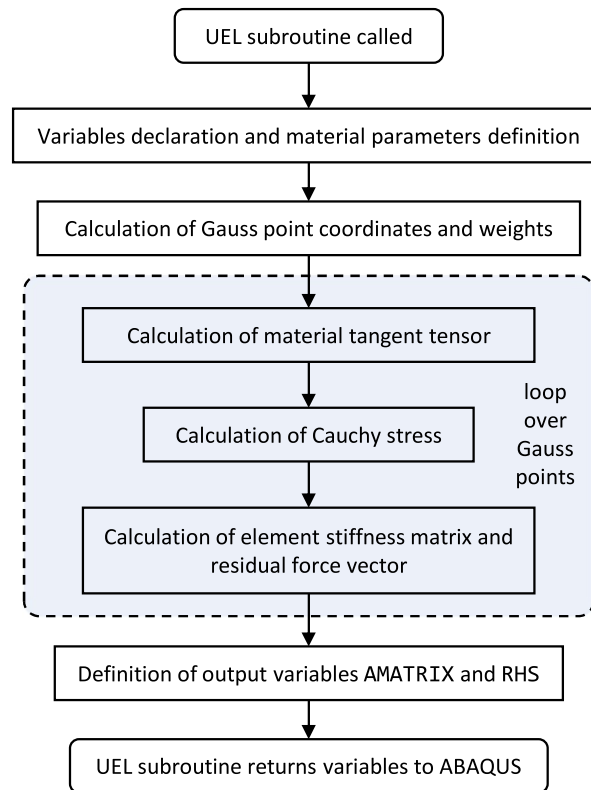
Fig. 3. A flowchart of the UEL subroutine.

At the beginning of the UEL, variables are declared and the material properties are defined by values passed in from an input file. According to the order of Gauss quadrature, the coordinates and weight of each Gauss point are calculated. Entering the Gauss loop, the basis functions and their derivatives, as well as the determinant of the Jacobian matrix are calculated. Then the material tangent tensor and the Cauchy stress are also calculated. At the end of the Gauss loop, the element matrix and the residual force vector are calculated through the Gauss quadrature scheme. Following the convention of ABAQUS, the element matrix is passed to AMATRIX, and the residual force vector is passed to the output variable RHS. With all the necessary output variables and state variables defined correctly, the UEL subroutine returns these variables to ABAQUS for assembling into the global stiffness matrix and the residual force vector. Then, the solver is called to solve the assembled linear algebraic equation system, yielding the solution for the current iteration. Following the Newton iteration approach, if the solution satisfies governing equation with a certain tolerance, this iteration step is said to be converged, and a new incremental load step will begin; otherwise, a new iteration step will begin until it exceeds the maximum number of iterations, in which case, the load step is decremented.

Since the element orientation and degrees of freedom of the user element may be incompatible with the setting of the visualization module, plotting of user elements is not supported in ABAQUS/CAE. However, all the solution and state variables information is enclosed in the user element subroutine. To visualize the results of user elements in the ABAQUS/Viewer, the dummy element method is adopted in this work. The dummy elements are generated by duplicating the original mesh with the same nodes but with very weak stiffness such that it has a negligible effect on the solution. The user elements can be overlaid with standard elements, and the nodal displacement of the standard element can be displayed, representing the deformation of the user elements.

4. Numerical examples

Units: Although it is straightforward to model the electro-growth problem in the SI units, the magnitude of material parameters between the mechanical and electrical fields varies significantly. Due to the substantial

Table 2
Units used in the present work for fundamental quantities.

Variables	Units
Length	millimetres (mm)
Mass	grams (g)
Time	seconds (s)
Electric potential	kilo Volts (kV)
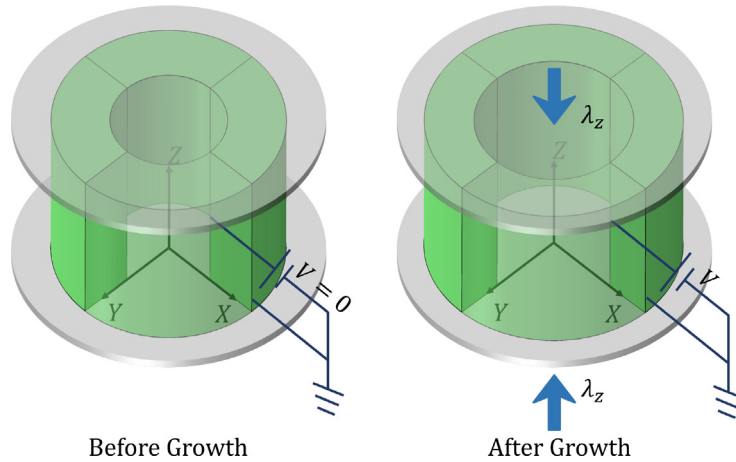
Fig. 4. The tubular structure is made of an electro-elastic solid with applied stretch λ_z in the axial direction and voltage in the radial direction.

differences in the magnitudes of parameters in elastostatic and electrostatic problems, the non-zero coefficients in the matrix system vary significantly as well. Such matrix systems pose serious challenges in obtaining numerical solutions. To overcome these numerical issues, we follow the practice of modelling with the units for the basic quantities (presented in [69]), as tabulated in Table 2.

Using the units in Table 2, permittivity of the free space and the shear modulus become $\epsilon_0 = 8.854 \times 10^{-12}$ F/m $= 8.854$ g mm/(kV^2 s^2) and $\mu = (\cdot)$Pa $= (\cdot)$ g/(mm s^2), respectively. Thus, the material parameters between the mechanical and electrical fields are in the same regime, making it easy to solve the matrix system under the Newton–Raphson scheme.

4.1. Verification with analytical solution

The accuracy of the developed UEL subroutine is at first verified by studying an example with an analytical solution discussed in [7]. Here, we consider the deformation of a circular tube under an axial stretch/compress in z-direction and with a prescribed electric potential on the inner and outer faces. The growth tensor is assumed to be a constant diagonal tensor. All the diagonal components are set such that the tube is under isotropic growth and is independent of any external electro-mechanical loads. As shown in Fig. 4, in the reference configuration, the tube occupies the region

$$R_i \leq R \leq R_o, \quad -\pi \leq \Theta \leq \pi, \quad 0 \leq Z \leq L, \tag{46}$$

while in the current configuration, the tube occupies the region

$$r_i \leq r \leq r_o, \quad -\pi \leq \theta \leq \pi, \quad 0 \leq z \leq l. \tag{47}$$

Under the isotropic growth and axial loading, the deformation gradient tensor, growth tensor, and elastic deformation tensor of the tube are written as

$$
\boldsymbol{F} = \begin{bmatrix} \frac{\partial r}{\partial R} & 0 & 0 \\ 0 & \lambda & 0 \\ 0 & 0 & \lambda_z \end{bmatrix},
$$
$$
\boldsymbol{F}^g = \begin{bmatrix} g & 0 & 0 \\ 0 & g & 0 \\ 0 & 0 & g \end{bmatrix}, \qquad \boldsymbol{F}^e = \begin{bmatrix} g^{-1}\frac{\partial r}{\partial R} & 0 & 0 \\ 0 & g^{-1}\lambda & 0 \\ 0 & 0 & g^{-1}\lambda_z \end{bmatrix},
\tag{48}
$$

where $\boldsymbol{F}^e$ is obtained by virtue of (3), g is the growth parameter in constant, $\lambda = r/R$ and $\lambda_z = l/L$. To enforce the incompressible constrain (6), we have

$$
\frac{\partial r}{\partial R} = g^3 \lambda^{-1} \lambda_z^{-1},
\tag{49}
$$

which further gives the geometrical relation

$$
R^2 - R_i^2 = g^{-3} \lambda_z \left(r^2 - r_i^2 \right).
\tag{50}
$$

To obtain some concrete results, the material is chosen as the ideal Neo-Hookean dielectric solid. The mechanical part of the strain energy function is given in (25), while the strain energy function corresponding to the electromechanical coupling is given in (26). Then, following the derivations in [7], the corresponding dimensionless voltage $\bar{V}$ is

$$
\bar{V} = \frac{\bar{r}_o \lambda_i \lambda_z^{-1} \ln \bar{r}_o}{\bar{R}_o - 1} \sqrt{\frac{1}{\bar{r}_o^2 - 1} \left(g^4 \lambda_o^{-2} - g^4 \lambda_i^{-2} + 2\, g \lambda_z \ln \frac{\lambda_i}{\lambda_o} \right)},
\tag{51}
$$

where $\bar{r}_o = r_o/r_i$, $\bar{R}_o = R_o/R_i$, $\lambda_i = r_i/R_i$ and $\lambda_o = r_o/R_o$. Using (50), the dimensionless voltage $\bar{V}$ can be rewritten in terms of $\bar{V}(\lambda_i, \bar{R}_o, \lambda_z, g)$. Thus, when $(\bar{R}_o, \lambda_z, g)$ are given, the relations of dimensionless voltage $\bar{V}$ and inner circumferential strain λ_i can be plotted.

In the numerical simulation, we consider a 3D model with the original height $L = 2$ mm, inner radius $R_i = 1$ mm and outer radius $R_o = 2$ mm. The relative permittivity is taken as $\epsilon_r = 5$, $\epsilon_0 = 8.854$ g mm/(kV^2 s^2), and the shear modulus is $\mu = 10^4$ Pa. For the sake of saving computational efforts, only a quarter of the tube is modelled, which is meshed into 2040 (20-node) hexahedral elements. To be consistent with the analytical results, the loading process is divided into two stages. In the first stage, growth and axial stretching/compression are applied to the tube while the external voltage remains zero. At the end of the first stage, both the growth field and axial stretching/compression reach the target values. For the second stage, non-zero voltage is applied on the surfaces of the tube while both the growth field and axial stretch/compress remain target values achieved at the end of the first stage.

To show the accuracy and efficiency of the developed UEL, two cases are simulated. In case 1, λ_z is set as 1.0 and the growth parameter g is set as (1.0, 1.1, 1.2, 1.3) respectively. In case 2, the growth parameter g is set as 1.0 and the λ_z is set as (0.8, 1.0, 1.1, 1.2), respectively. The electro-response of the tube at certain constant magnitudes of $\bar{V}$ is shown in Fig. 5, where $g = 1.0$ and $\lambda_z = 1.0$. It can be seen that the application of voltage leads to the radial expansion of the tube.

The results of inner circumferential strain λ_i versus dimensionless voltage $\bar{V}$ at the second loading stage are shown in Fig. 6, where the solid lines are analytical results, and the dots are numerical results. As shown in Fig. 6, the results obtained from the developed UEL are in excellent agreement with the analytical solutions. In all cases, we observed that the inner circumferential strain λ_i shots to infinity with the increase of dimensionless voltage $\bar{V}$. The increase of g also raises the threshold of $\bar{V}$ leading λ_i to infinity. However, the threshold is lowered by increasing λ_z.

To further demonstrate the accuracy of the developed UEL, the stress components in the tube are extracted by specifying parameters g, V and λ_z. The distributions of the stress components along the radial directions are shown in Fig. 7, where the solid, dashed, and dotted lines are analytical results of $\bar{\sigma}_r$, $\bar{\sigma}_\theta$ and $\bar{\sigma}_z$ respectively; the circular, rectangular, and triangle dots are numerical results of $\bar{\sigma}_r$, $\bar{\sigma}_\theta$ and $\bar{\sigma}_z$ respectively. $\bar{\sigma}_r$ is relatively small compared with the other two stress components $\bar{\sigma}_\theta$ and $\bar{\sigma}_z$, and it is zero at the inner and outer surfaces. The increase of g can reduce the magnitude of all the stress components.
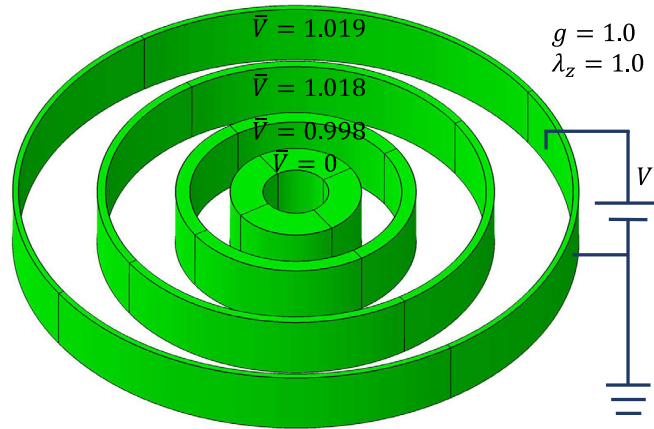
Fig. 5. The expansion of the tube due to the external electric stimulus when $g = 1.0$ and $\lambda_z = 1.0$.
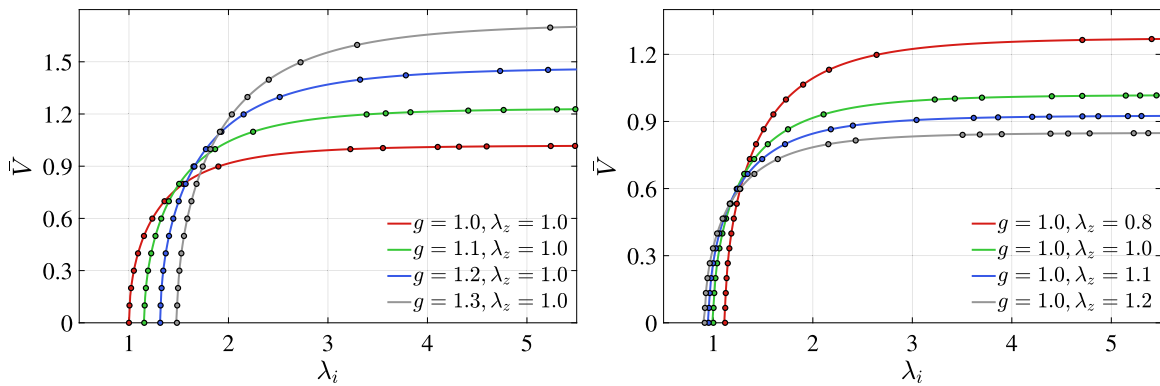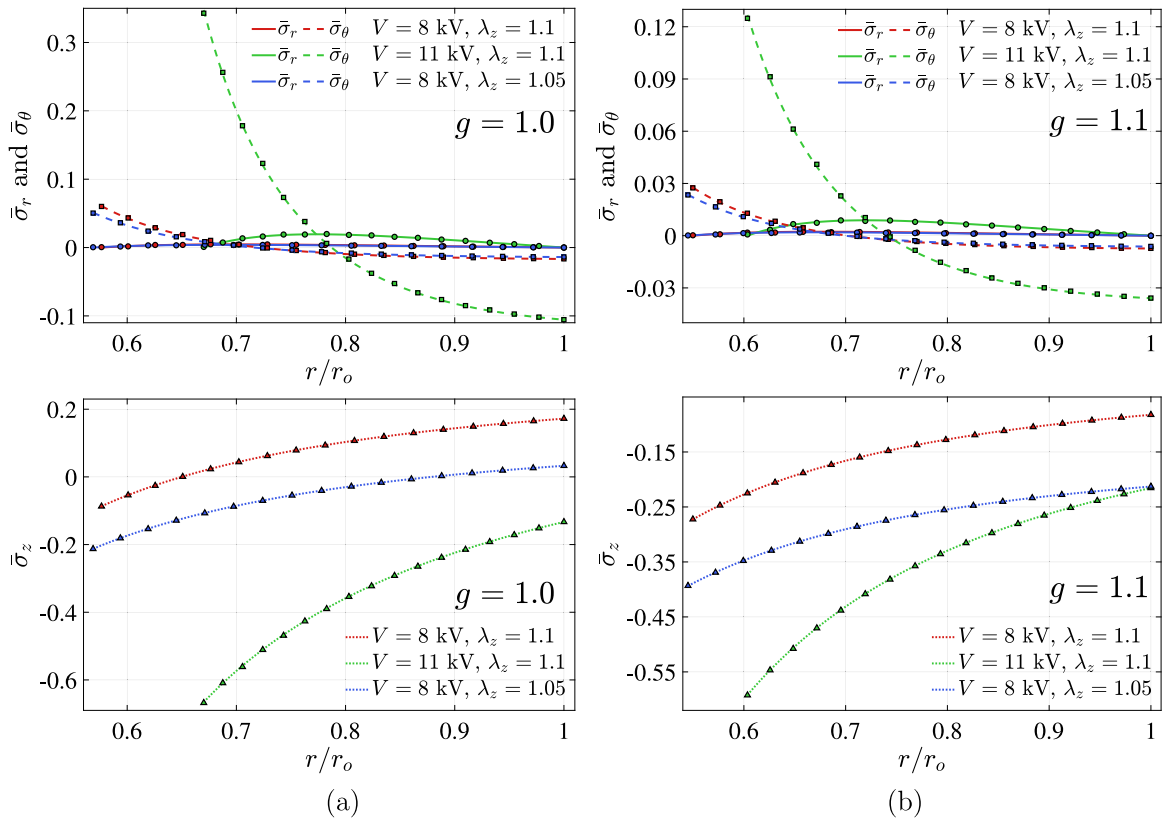

Fig. 6. Comparison of analytical result (solid lines) and numerical result (dots) of inner circumferential strain λ_i versus dimensionless voltage $\bar{V}$ at loading stage 2.
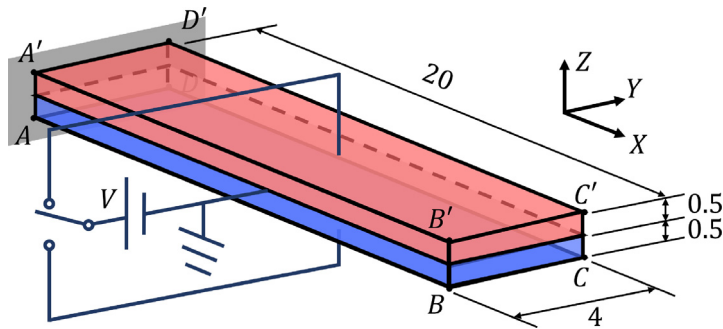
4.2. The bi-layer bending actuator

In this example, we demonstrate the suitability and effectiveness of the proposed finite element framework for electro-growth actuators undergoing a bending deformation. For this purpose, we consider a thin bi-layer actuator whose geometry and boundary conditions are as shown in Fig. 8, where the length of the beam is $|AB| = 20$ mm, thickness $|AA'| = 1.0$ mm and width $|BC| = 4$ mm.

The thickness of each layer is 0.5 mm. The interface between the two layers is grounded, and a positive voltage of $\phi = 4$ kV is applied on the top or the bottom face. The left side of the beam ($ADD'A'$) is fixed elastically, making this a bi-layer cantilever. The material model is taken as Neo-Hookean with a shear modulus of $\mu = 10^4$ Pa and a bulk modulus $\kappa = 10^9$ Pa, and the permittivity $\epsilon = \epsilon_0\epsilon_r = 8.854 \times 5$ g mm/(kV^2 s^2). The 3D model is meshed into $40 \times 8 \times 8$ elements in X, Y and Z directions. To demonstrate the efficiency of the UEL subroutine, we introduce two loading cases, with the total duration of the simulated electro-growth process is 2. In case 1, growth functions and electric stimuli are applied separately in different time intervals, while in case 2, growth functions and electric stimuli are applied simultaneously.

Case 1: In the first stage $t \in [0, 1]$, the growth function increase linearly from identity $\boldsymbol{I}$ to $\boldsymbol{F}_t^g = \text{diag}(\pi/2 + Z\pi/40, 1, 1)$, while the external electric potential remains zero. This growth tensor will generate a quarter of a cylinder with a bending angle of 90° and an outer radius of 20, which is calculated according to the formulations

Fig. 7. Comparison of analytical result (lines) and numerical result (dots) of stress components $\bar{\sigma}_r$, $\bar{\sigma}_\theta$ and $\bar{\sigma}_z$. The solid, dashed, and dotted lines are analytical results of $\bar{\sigma}_r$, $\bar{\sigma}_\theta$ and $\bar{\sigma}_z$ respectively; the circular, rectangular, and triangle dots are numerical results of $\bar{\sigma}_r$, $\bar{\sigma}_\theta$ and $\bar{\sigma}_z$ respectively. Different growth parameters are considered: (a) $g = 1.0$; (b) $g = 1.1$.

Fig. 8. A bi-layer bending actuator: problem setup for the 3D model.

obtained in [75]. In the second stage $t \in [1, 2]$, the growth function remains unchanged as $\boldsymbol{F}_t^g$, while the electric potential increase linearly from 0 to $\phi = 4$ kV.

Case 2: During time regime $t \in [0, 2]$, the growth function increase linearly from identity $\boldsymbol{I}$ to $\boldsymbol{F}_t^g = \text{diag}(\pi/2 + Z\pi/40, 1, 1)$, while the electric potential increase from 0 to $\phi = 4$ kV. It is expected that, irrespective of the loading case, the bending angle of the beam should be the same at the end since the prescribed growth tensor $\boldsymbol{F}_t^g$ and the applied potential ϕ is the same at the end of each case.

The simulation results are shown in Fig. 9, including bending angle (a), and deformed shapes of the beams in (b) and (c). As presented in Fig. 9(a), the bending angle increases linearly from 0 to 90° in the first stage of case 1
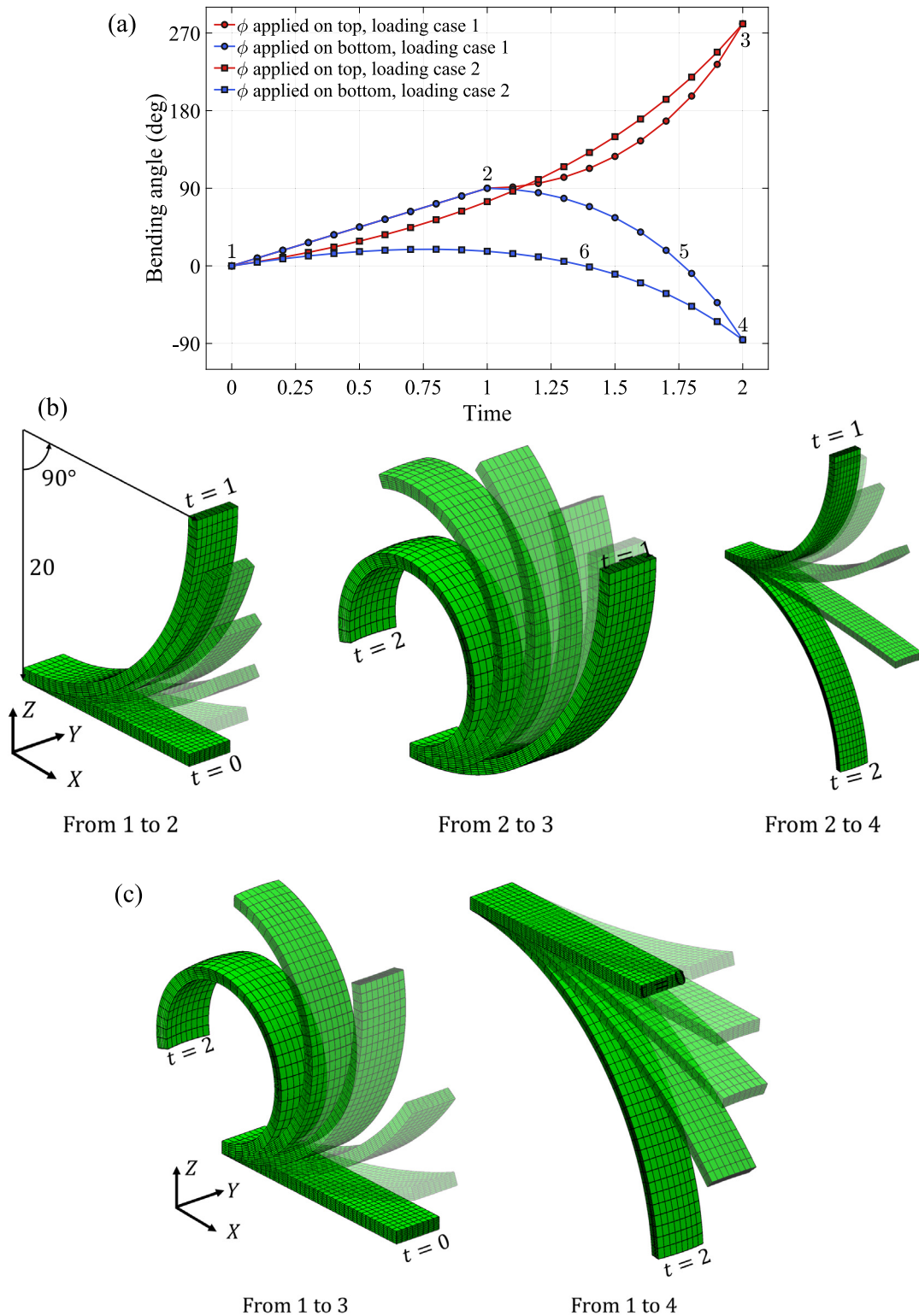
Fig. 9. Numerical results of a bending actuator in 3D: (a) bending angle of the beam during time $t \in [0, 2]$; (b) deformation of the actuator in loading case 1; (c) deformation of the actuator in loading case 2. (For interpretation of the references to colour in this figure legend, the reader is referred to the web version of this article.)
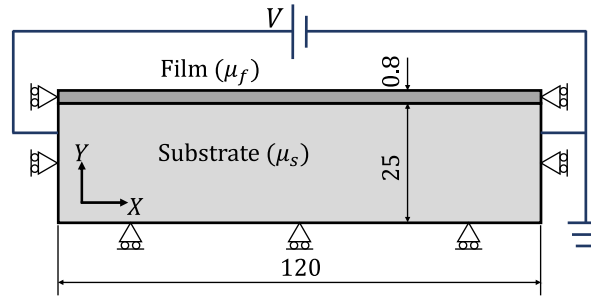
Fig. 10. The stiff film/soft substrate structure: geometry and boundary conditions.

(i.e., from point 1 to 2) due to pure growth, generating a quarter of cylinder with an outer radius 20. During time $t \in [0, 1]$, the curves with circle markers are coincident as the beams are experiencing the same pure growth process. Then the two curves branch at $t = 1.0$: the electric potential ϕ applied on the top face drives the bending angle from point 2 to point 3, while the electric potential ϕ applied on the bottom face causes the drop of bending angle down to point 4. As for loading case 2 (see the curves with square markers), growth fields and electric potential are applied simultaneously on the beam. Upward bending deformation is observed when the electric stimulus is applied on the top face, in which the bending angle increases from points 1 to 3 monotonically. When the electric stimulus is applied on the bottom face, the beam bends up first and then bends down, with the bending angle reaching a maximum $19.22°$ at time 0.8, then drops down to point 4. In both cases, we observed the electric stimulus on the top face of the beam leads to upward bending deformation, while the electric stimulus on the bottom face of the beam results in downward bending deformation.

The beams with electric stimulus on the bottom face (see the curves in blue) experience balancing in terms of the bending angle, where the bending angle becomes $0°$ again at point 5 in separate loading and point 6 in simultaneous loading. The effect of the growth field and the electric stimulus is balanced in this state, where the total contribution to the bending angle is zero. Notice that the beam is elongated in the balancing state due to growth compared with the reference configuration.

This example shows that the bending angle can be controlled by differential volumetric growth through a prescribed growth field or applied electric field, or a combination of both.

4.3. Wrinkling of a stiff film/soft substrate structure in plane strain condition

To assess how electric potential can influence the wrinkling pattern on a surface induced by growth, we simulate the post-buckling instabilities of a stiff film/soft substrate structure under an external electric stimulus. In this example, the structure is assumed to be in plane strain condition. The geometry and boundary conditions of the cross-section of the structure are shown in Fig. 10. The sample consists of a hard film on the top of a soft substrate, with the shear moduli of μ_f and μ_s, respectively. The external electric potential is specified on the left side of the sample, and it is grounded on the right side.

The material of the sample is the ideal Neo-Hookean dielectric material with permittivity $\epsilon = 44.27$, shear moduli of $\mu_f = 299.98$ and $\mu_s = 2.9998$ such that the ratio of shear modulus for the film and substrate as $\mu_f/\mu_s = 100$. Growth is prescribed in the X and Y directions, such that the growth tensor is $\boldsymbol{F}^g = \text{diag}(g, g, 1)$, where g is a constant parameter.

The film and substrate are meshed with 300×4 and 300×50 C3D20 elements, respectively. To trigger the initiation of the wrinkle pattern, a displacement perturbation is applied on the sample at the beginning of the first load step. To obtain the nodal displacement perturbation, a linear buckling analysis is conducted, from which we obtained the displacement field of all nodes in different buckle modes. An appropriate scaling factor is multiplied to the displacement field of the selected mode, such that the magnitude of the applied perturbation is large enough to trigger instability without affecting the accuracy of the result. Growth parameter g is set as 1.05, 1.10, 1.15, and 1.20, respectively. The selected linear buckling mode is a 5-period waves with a scaling factor of 0.05. The applied electric potential on the left end is 145 kV, and the right side is grounded. To have a better understanding of the effect of the electric stimulus, growth and electric potential are applied separately in the post-buckling analysis, i.e., in time regime $t \in [0, 1]$, the growth function increases linearly from identity $\boldsymbol{I}$ to $\boldsymbol{F}^g_t = \text{diag}(g, g, 1)$, while
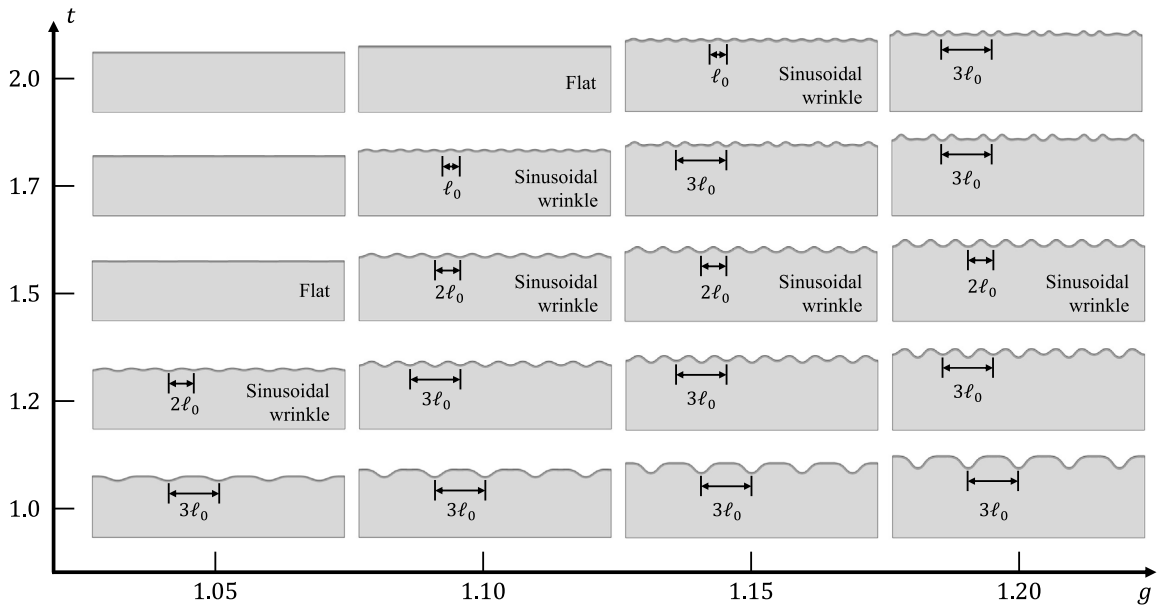
Fig. 11. A cross-section of the stiff film/soft substrate structure: wrinkle pattern of the sample when time t is 1.0, 1.2 1.5, 1.7 2.0, and g is set as 1.05, 1.10, 1.15, and 1.20, respectively. The wavelength of the samples at time $t = 1.0$ is denoted as $3\ell_0$.

the external electric potential remains zero; in time regime $t \in [1, 2]$, the growth function remains unchanged as F_t^g, while the electric potential increases linearly from 0 to $\phi = 145$ kV. When external voltage is applied, the sample has the tendency to shrink in the X direction. However, due to the constraint $u_x = 0$ in the left and right sides of the sample, this tendency of shrinking is eliminated by induced residual tension stress in the X axis. The evolution of the wrinkle pattern in the sample is shown in Fig. 11.

At the time $t = 1.0$, i.e., at the end of the pure growth stage, all the samples have 5 waves (not sinusoidal), which is consistent with the applied linear buckling perturbation. Then external electric stimulus starts to play a role from $t = 1.0$, leading to variations in the number of wrinkles. At the time $t = 1.2$, the number of wrinkles is doubled to 10 in the case of $g = 1.05$. At the time $t = 1.5$, the number of wrinkles is also doubled to 10 in the cases of $g = 1.10$, $g = 1.15$ and $g = 1.20$. The number of wrinkles is tripled to 15 in the case of $g = 1.10$ at time $t = 1.7$, and this tripling moment is $t = 2.0$ for the case of $g = 1.15$. The film surfaces are flat at $t = 2.0$ when $g = 1.05$ and $g = 1.10$.

To qualify the effect of voltage on the wrinkle pattern, the amplitude of the film is calculated by subtracting coordinate $Y_{\max} - Y_{\min}$ in the top surface of the film at each load step. The variation of the amplitude with time in the film is shown in Fig. 12. In the pure growth stage $t \in [0, 1]$, the amplitude of each sample increases with time and is positively correlated with the growth parameter g. Due to the applied voltage, a sharp drop of amplitude is observed in the doubling and tripling wrinkle transformation. In the case of $g = 1.05$ and 1.10, the film becomes flat in the end. Although wrinkles are still observed at $t = 2$ when the growth parameter is large ($g = 1.15$ and 1.20), it is expected that they eventually flatten with a further increase in external voltage. From this example, we see that *the growth parameter can promote the formation of wrinkles, while external electric potential can suppress wrinkles*.

4.4. Wrinkling of a stiff film/soft substrate structure in 3D

To understand the mechanism of pattern transformation, a simulation of a 3D growing stiff film/soft substrate structure under an external electric stimulus is conducted as an extension of the example in 4.3. For the sake of saving computational efforts, only a quarter of the sample is modelled. The geometry and boundary condition of the quarter of the 3D sample are shown in Fig. 13.

As shown in Fig. 13, both the length and width of the sample are 60. The thickness of the hard film and the soft substrate are 0.8 and 25, respectively. The external electric potential is specified on the left side (face $ADD'A'$) of
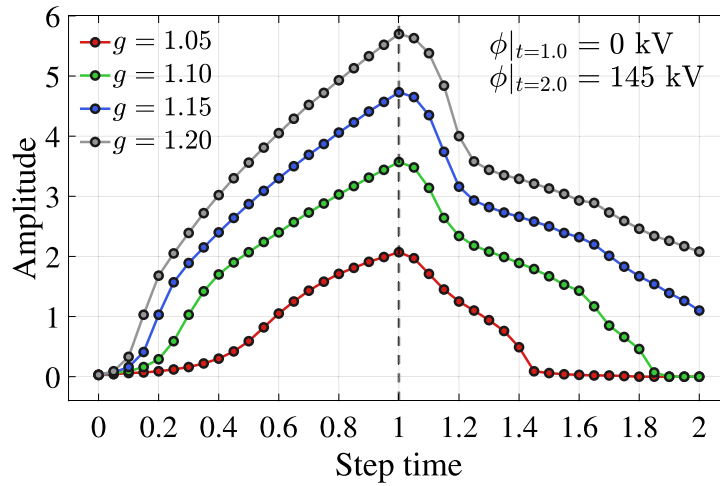
Fig. 12. The amplitude of the top surface of the hard film: amplitude of the film when g is set as 1.05, 1.10, 1.15, and 1.20, respectively, in time regime $[0, 2]$.
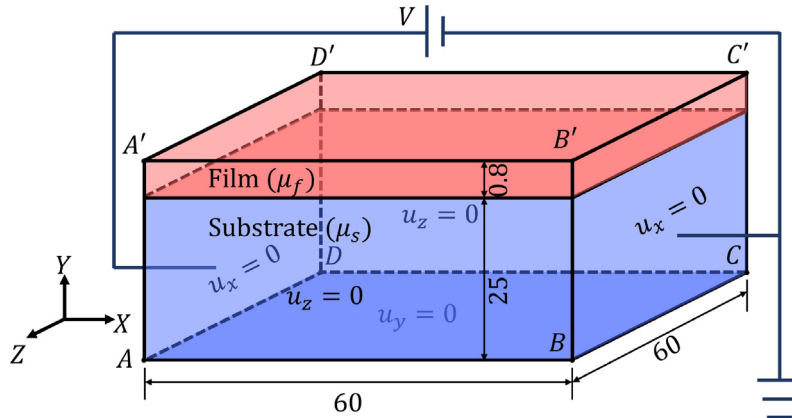

Fig. 13. Geometry and boundary conditions of a quarter of the stiff film/soft substrate structure.

the sample, and it is grounded on the right side (face $BCC'B'$). Displacement in the z direction is constrained in the bottom face (face $ABCD$). We have $u_x = 0$ in left and right side, and $u_z = 0$ in face $ABB'A'$ and $DCC'D'$. The material of the sample is taken as ideal Neo-Hookean dielectric material with permittivity $\epsilon = 44.27$ g mm/(kV^2 s^2). We set the shear modulus of the film and substrate as $\mu_f = 1000$ Pa and $\mu_s = 10$ Pa such that the ratio of shear modulus for the film and substrate as $\mu_f/\mu_s = 100$. Growth of the sample is assumed to be isometric, i.e., $\boldsymbol{F}^g = g\boldsymbol{I}$.

The quarter of the sample is meshed into 15 300 (20-node) hexahedral elements. To trigger the initiation of the wrinkle pattern, a nodal displacement perturbation is applied on the sample at the beginning of the first load step. Two of the first five modes from linear buckling analysis are chosen as the displacement perturbation with the scaling factor 0.1. The applied electric potential on the left is 50 kV. To have a better understanding of the effect of the electric stimulus, growth and electric potential are applied separately in the post-buckling analysis, i.e., in time regime $t \in [0, 1]$, the growth function increases linearly from identity $\boldsymbol{I}$ to $\boldsymbol{F}_t^g$ ($\boldsymbol{F}_t^g = g\boldsymbol{I}$), while the external electric potential remains zero; in the time regime $t \in [1, 2]$, the growth function remains unchanged as $\boldsymbol{F}_t^g$, while the electric potential increases linearly from 0 to $\phi_t = 50$ kV. Configurations and displacement (U_y) contours of the sample during the electric loading process ($t \in [1, 2]$) are shown in Fig. 14, where the growth parameter g for Fig. 14(a) and (b) is 1.023 and 1.024, respectively.

We can see that the wrinkles are suppressed in both Fig. 14(a) and (b), where the wrinkles are highest at time $t = 1.0$ due to growth, and then they are nearly flattened at the end of the electric loading $t = 2.0$. Apart from suppression of wrinkles, pattern transformation is also observed in both Fig. 14(a) and (b). For Fig. 14(a), there are two cusps in the area marked with A at time $t = 1$, which finally merge into one cusp at time $t = 2.0$. As for the cusp in the area marked with B, movement from the inner side to the outer side is observed. For Fig. 14(b), the
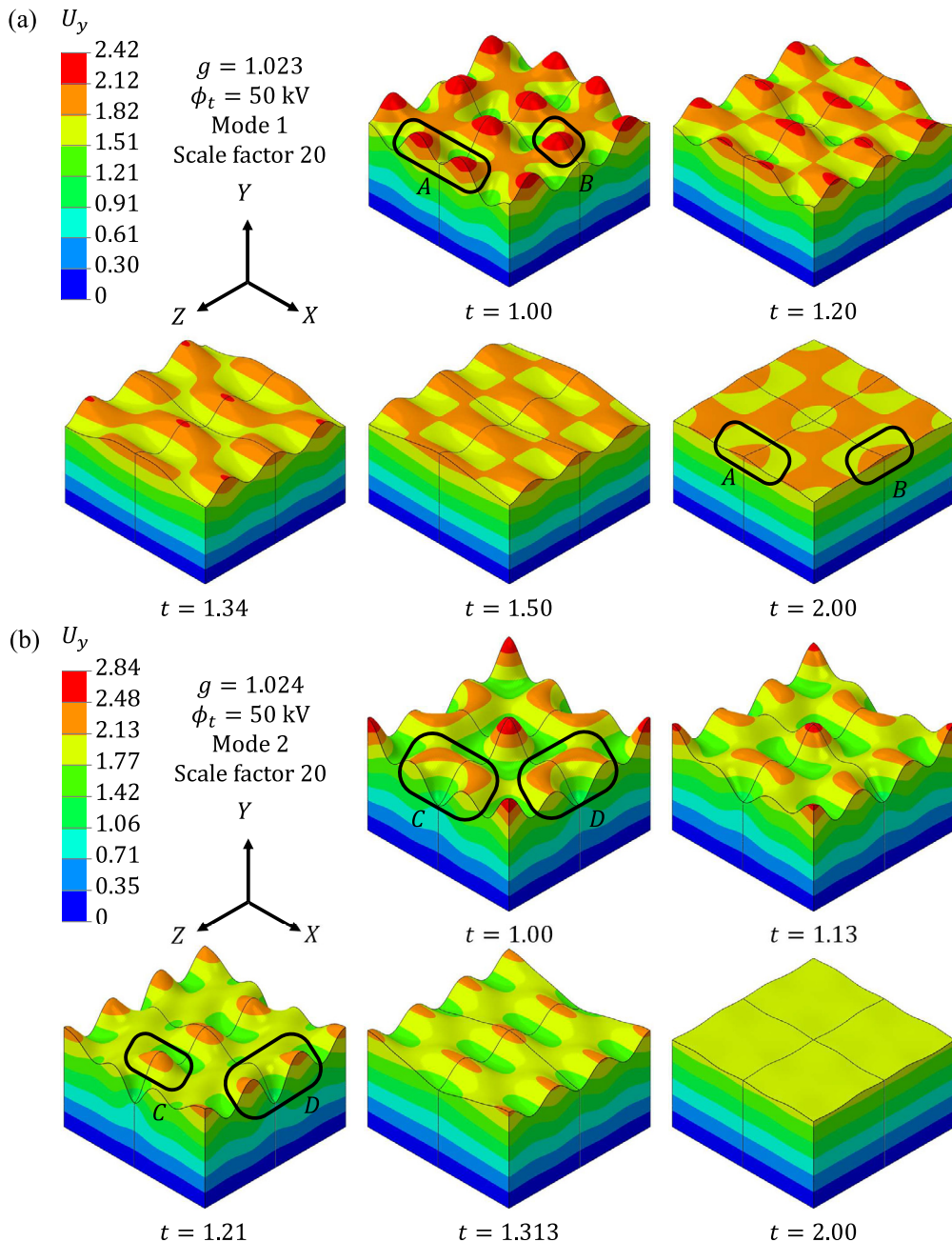
Fig. 14. Configurations and displacement (U_y) contours of the sample during the electric loading process ($t \in [1, 2]$), where the whole sample is generated by duplicating the quarter of the sample in X and Z directions with the deformation scale factor 20.

shapes in the area marked with C and D at time $t = 1$ are similar. However, the pattern evolutions of areas C and D are different. Area C consists of one cusp, while area D consists of two cusps at time $t = 1.21$.

From this example, we see that the external electric potential not only affects pattern formulation but also can suppress wrinkles. The electric field can be explored further as a potential control mechanism for controlling patterns in growing elastic solids.

4.5. Response of a growing tube

To figure out the mechanism of the morphological remodelling under the external electric stimulus, post-buckling analyses are conducted on a long tube. Similar to the geometry and boundary condition setting in 4.1, the long tube occupies the region $R_i \leq R \leq R_o$, $-\pi \leq \Theta \leq \pi$, $0 \leq Z \leq L$. In the numerical simulation, we consider a 3D model with the original height $L = 5$ mm, inner radius $R_i = 1$ mm and outer radius $R_o = 1.5$ mm. The relative permittivity is taken as $\epsilon_r = 5$, $\epsilon_0 = 8.854$ g mm/(kV^2 s^2), and the shear modulus is $\mu = 10^4$. For the sake of saving computational efforts, only a quarter of the tube is modelled, which is meshed into 12400 (20-noded) hexahedral elements. The axial stretching/compression parameter λ_z is set as 1.0. Growth parameter g is set as 1.1, 1.2, and 1.3, respectively. Similar to the previous examples, growth and electric fields are applied separately in two different load steps. The growth tensor is isotropic. For comparison, we introduce two different cases for the application of voltage. In case 1, the electric potential difference is along the radial direction, where the inner surface is applied with voltage $\phi_t = 6$ kV, and the outer surface is grounded. In case 2, an electric potential difference is applied along the axial (Z) direction, where the top face is applied with a voltage $\phi_t = 50$ kV and the bottom face is grounded. To trigger the initiation of instability, a displacement perturbation is applied at the beginning of the first load step with a scale factor of 0.01. Two buckle modes are selected as the geometry imperfection from the first five modes of linear buckling analysis.

For case 1, the simulation results of the two modes are shown in Figs. 15 and 16, respectively. The applied geometry imperfections of case 1 are shown in the sub-figure in Figs. 15(a) and 16(a), which are in the form of non-axisymmetric and axisymmetric shape, respectively. To qualify the deformation, the Y-amplitude of a line locating at $X = 0$ on the outer surface is presented in Figs. 15(a) and 16(a), which are marked with thick solid lines in their subfigures. The shape of this line on the outer surface is plotted in Figs. 15(b) and 16(b) to show the wrinkles of the tube at some key points of simulation, i.e., M_1–M_3 and N_1–N_3 for non-axisymmetric geometry imperfection, and P_1–P_3 and Q_1–Q_3 for axisymmetric geometry imperfection.

As shown in Figs. 15(a) and 16(a), Y-amplitude of line $X = 0$, $Y = R_o$ increases with time during the growth process ($t \in [0, 1]$), and reaches to M_1, M_2 and M_3 for mode 1 and P_1, P_2 and P_3 for mode 2 at $t = 1$ for growth parameter $g = 1.1$, $g = 1.2$ and $g = 1.3$ respectively. In both tubes under two different geometry imperfection modes, the amplitude at the end of the growth process ($t = 1.0$) positively correlates with the growth parameter g. Then, by applying an external electric stimulus in the radial direction, the Y-amplitude of line $X = 0$, $Y = R_o$ increases with voltage and reaches N_1, N_2 and N_3 for mode one and Q_1, Q_2 and Q_3 for mode two at the end of simulation for growth parameter $g = 1.1$, $g = 1.2$ and $g = 1.3$, respectively. We can clearly see that the external voltage along the radial direction promotes wrinkles. All the simulations diverged before $t = 2.0$, and there is such a trend that the Y-amplitude of the line located at $X = 0$ on the outer surface shoots to infinity. The larger the growth parameter, the earlier the simulation crashes, i.e., this upper limit of voltage decreases with the growth parameter g, which is similar to the previous results presented in Fig. 6.

We choose the stress component σ_z to analyse the behaviour of the growing tubes under external voltage as the magnitude of σ_z is much larger than σ_r and σ_θ. Figs. 17 and 18 present the stress σ_z distribution regarding to imperfection mode one and mode two, respectively.

From Figs. 17 and 18, we can see residual stress is induced by growth at time $t = 1$. When parameter g is small ($g = 1.1$), the stress field of σ_z due to growth is uniformly distributed. The uniform distribution of stress component σ_z at time $t = 1.0$ no longer exists when we increase the growth parameter. Furthermore, applying external voltage along the radial direction exacerbates this non-uniformity of the stress field, where the minimum of stress is decreased and the maximum is increased, resulting in the obvious wrinkling surfaces of the tubes.

In case 2, the electric potential is applied in the axial (Z) direction, and the growth parameter g is also set as 1.1, 1.2 and 1.3. The Y-amplitude of the line at $X = 0$ and $Y = R_o$ is presented in Fig. 19(a) and (b) for mode 1 and 2 respectively.

Both Fig. 19(a) and (b) show that the y-amplitude reaches the maximum at time $t = 1.0$ due to growth. By applying the external voltage, the y-amplitude decreases with time, suggesting that wrinkles are suppressed by the external voltage along the axial direction. Although the surfaces of the tubes are not completely flat at $t = 2.0$, it is expected that a larger external voltage will flatten the surfaces.

Compared with case 1, the deformation on the outer surface in case 2 is significantly different. For further investigation, we plot the σ_z along line $X = 0$ and $Y = R_o$. As shown in Fig. 20, σ_z distribution of this line are presented for point M_1–M_3, N_1–N_3, G_1–G_3 and P_1–P_3, Q_1–Q_3, H_1–H_3.
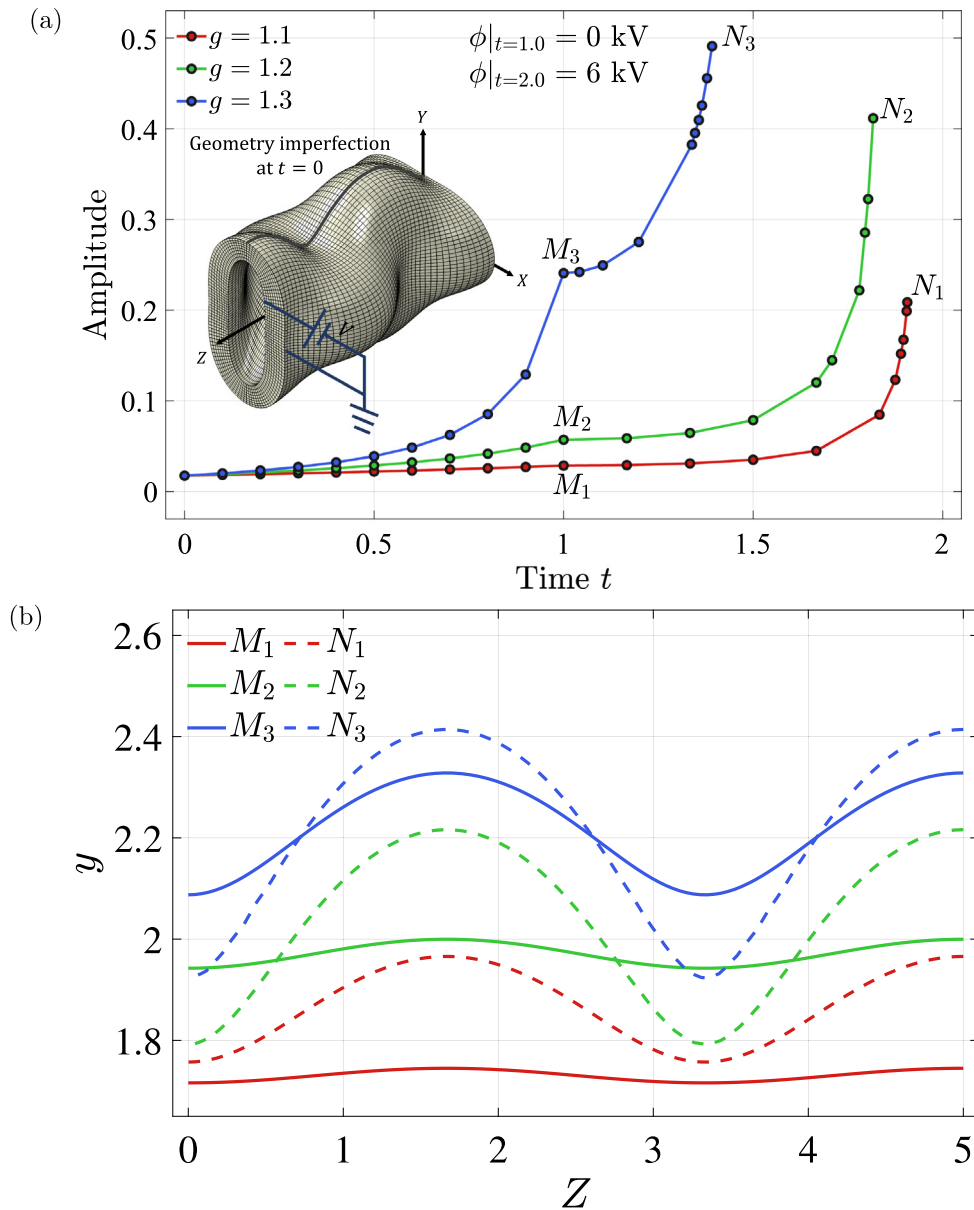
Fig. 15. Simulation results of the tube with radial electric potential difference and geometry imperfection mode 1. (a) the Y-amplitude of line $X = 0$ on the outer surface and geometry imperfection applied at time $t = 0$; (b) the shape of line $X = 0$ on the outer surface at time $t = 1$ (solid lines) and at the end of simulation (dashed lines).

At the end of the growth process, residual stress is accumulated due to mechanical constraints in the two ends $Z = 0$ and $Z = L$. When growth parameter is large, the fluctuation of stress distribution is obvious. In the presence of radial voltage, this fluctuation is enhanced, leading to the non-uniformity of stress distribution. However, this fluctuation is suppressed under axial voltage, showing that the residual stress is relaxed.

By investigating the two loading cases of tubes, we observed that voltage could increase or suppress wrinkles. Response of wrinkles mainly depends on stress redistribution inside the tube owing to the loading positions of external voltage. For case 1, the stress component in the Z direction σ_z is decreased to negative, as demonstrated in Fig. 7. The analogy to applying compression in the axial direction, the external voltage along the radial direction causes the non-uniformity of σ_z, leading to the promotion of wrinkles and instability. However, for case 2, σ_z
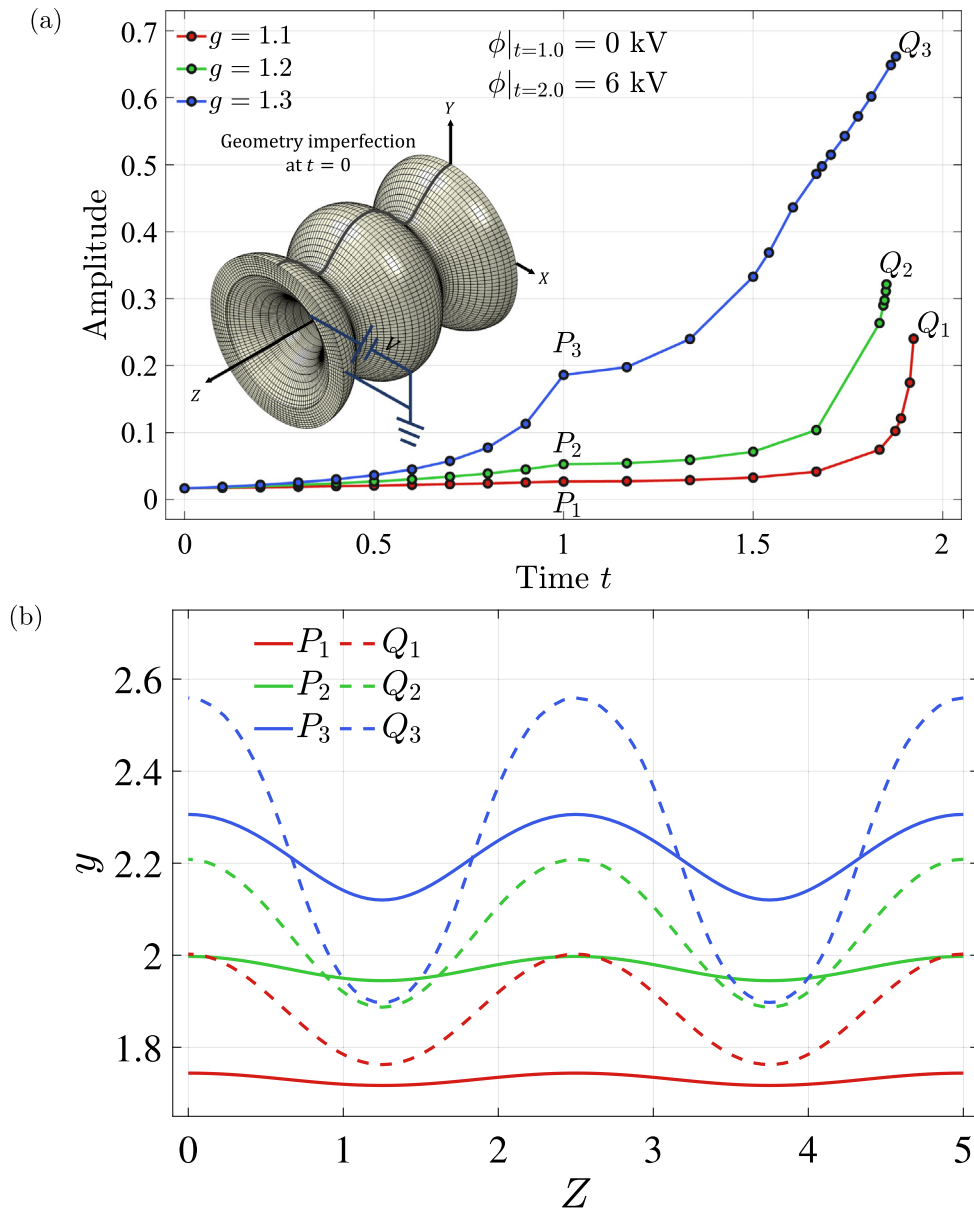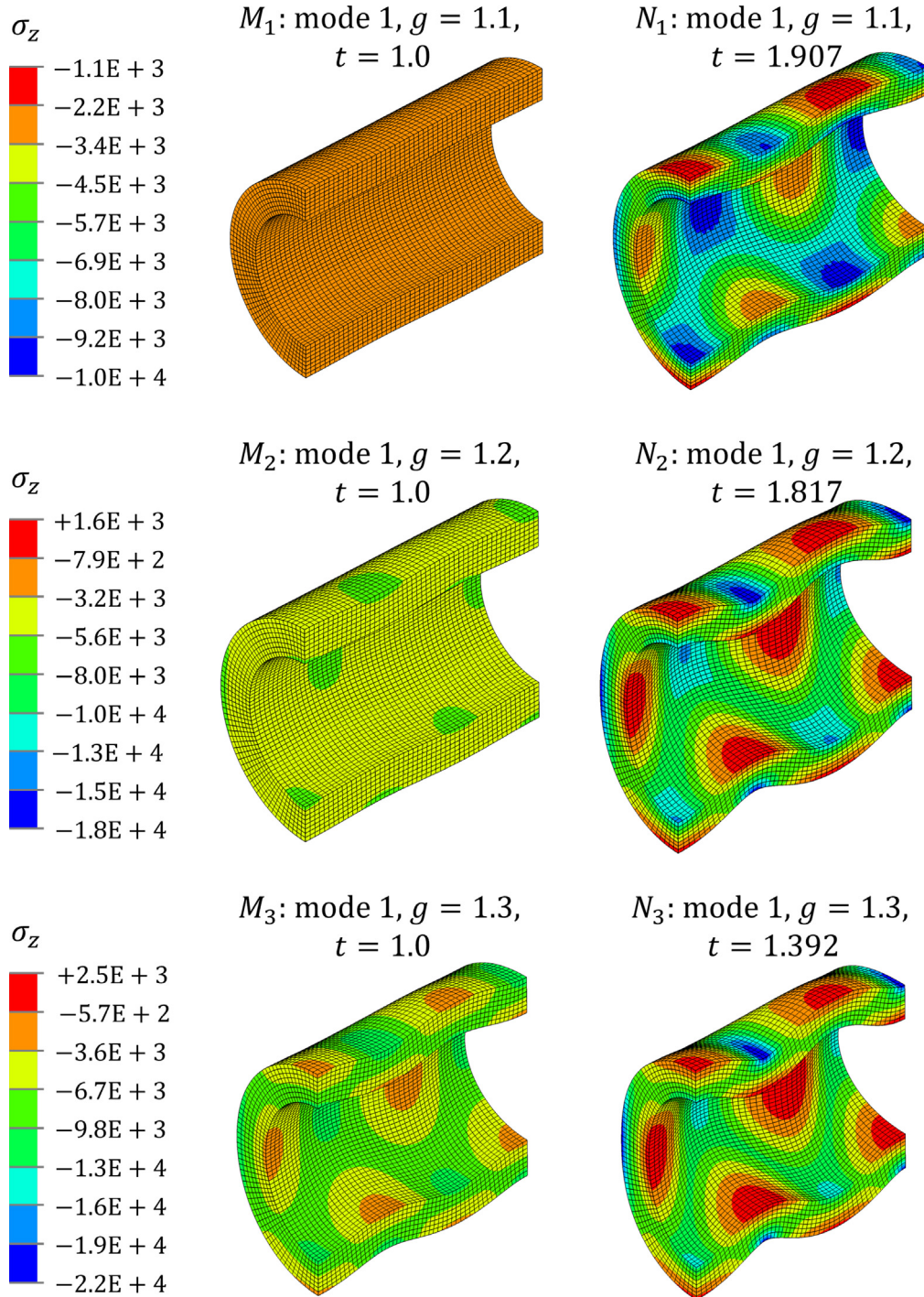
Fig. 16. Simulation results of the tube with radial electric potential difference and geometry imperfection mode 2. (a) the Y-amplitude of line $X = 0$ on the outer surface and geometry imperfection applied at time $t = 0$; (b) the shape of line $X = 0$ on the outer surface at time $t = 1$ (solid lines) and at the end of simulation (dashed lines).

increases to positive, which is similar to applying tension in the axial direction, resulting in the suppression of wrinkles.

5. Conclusions

In this work, we proposed a finite element framework for simulating the coupled response of electro-elastic materials under growth effects and applied electric field. The novel aspects of this study are the extension of a recently published three-field mixed displacement-pressure-potential formulation to model coupled electro-mechanical growth in soft incompressible materials and valuable insights gained into the effect of electric and growth fields on the mechanical deformation in soft materials. The computer simulations are realized through a

Fig. 17. Stress σ_z distribution of the tube with radial electric potential difference and geometry imperfection mode 1 at moments M_1–M_3 and N_1–N_3.

user element subroutine in ABAQUS. The mixed hexahedron element (Q2/Q1) is employed to account for true incompressibility and model the large deformation behaviour accurately using coarse meshes. To demonstrate the accuracy and effectiveness of the proposed numerical framework, we consider several numerical examples, such as tubular and stiff film/soft substrate structures.
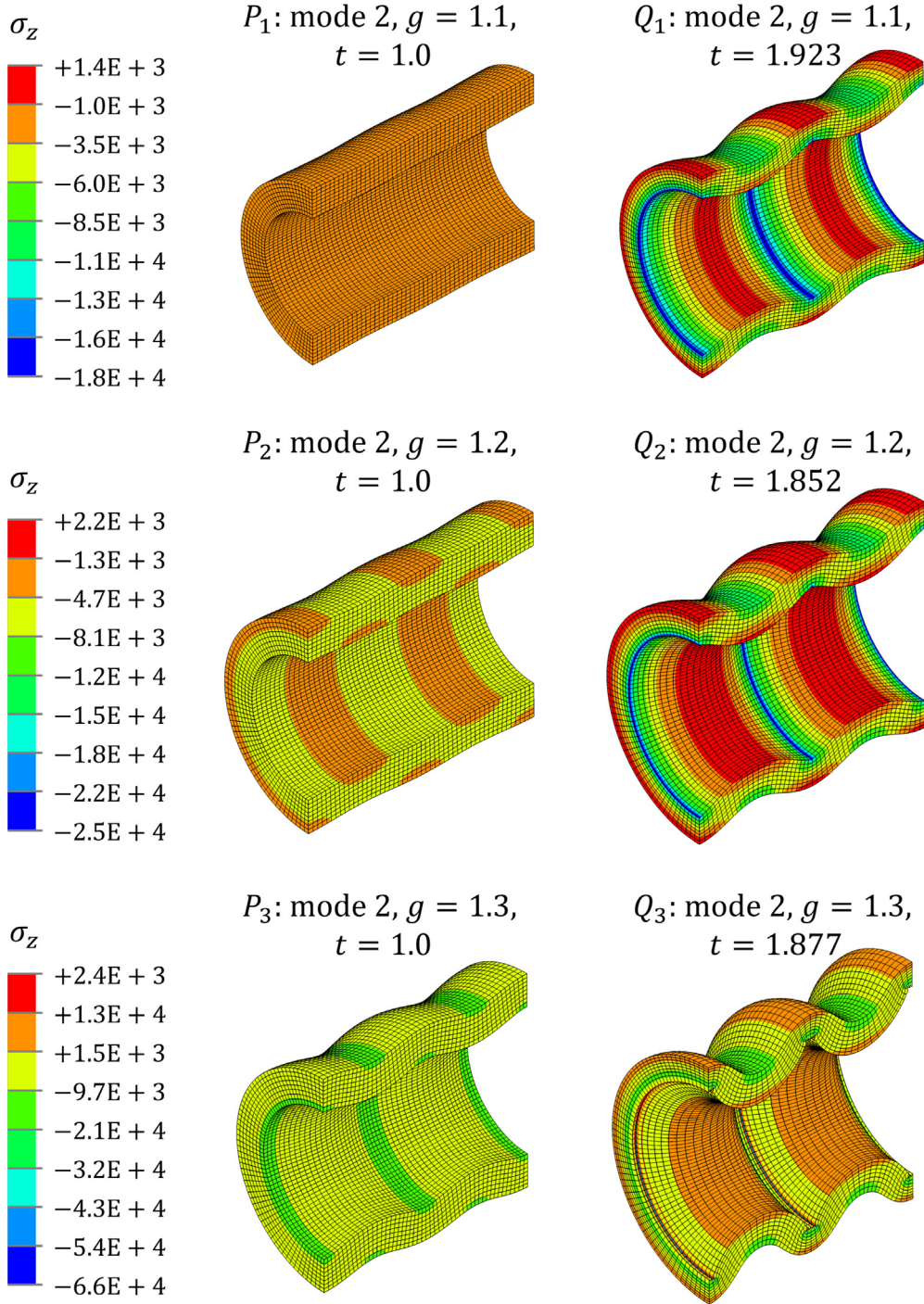
Fig. 18. Stress σ_z distribution of the tube with radial electric potential difference and geometry imperfection mode 2 at moments P_1–P_3 and Q_1–Q_3.

By introducing the growth field, the volume of growing electro-elastic material is adjustable, making up for a deficiency of traditional dielectric material that the overall deformation is isochoric. The numerical framework is first validated using the example of the tubular structure under an axial strain and a radial voltage, for which the analytical solution exists. Further numerical experiments on this example revealed upper limits for the applied voltage in the radial direction, corresponding to the axisymmetric collapse of the tubular structure with a certain
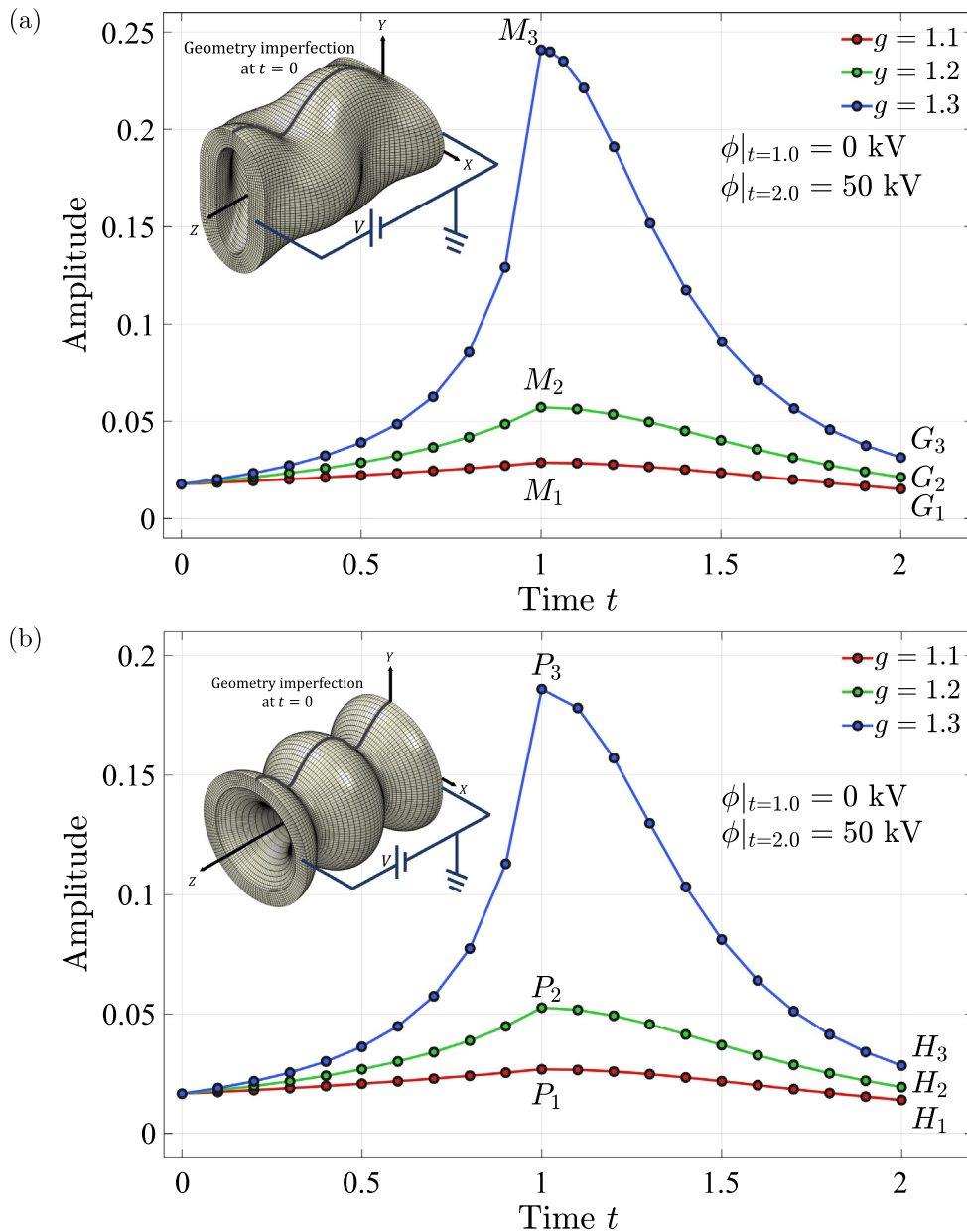
Fig. 19. The Y-amplitude of line $X = 0$ on the outer surface of the tube with axial electric potential difference and geometry imperfection applied at time $t = 0$: (a) mode 1 (b) mode 2.

axial stretch and growth factor. Using the example of a bilayer cantilever beam, we demonstrated the flexibility of developing novel shape programming schemes by combining the effects of growth and electric fields to control the bending deformation of beam.

Investigation of the post-buckling behaviour of tubes and stiff film/soft substrate structures offered key insights into the formation and attenuation/suppression of wrinkles. The post-buckling results of stiff film/soft substrate structures show that the surface pattern formation can be guided or controlled by an external voltage. Pattern transition is observed during the electric loading process: *the number of the wrinkles is doubled or tripled by the applied voltage in the plane strain model, and complex pattern evolution such as merging, split, and movement of cusps are demonstrated in the 3D model of stiff film/soft substrate structure.* The example of a long tube suggests that the voltage can not only suppress but also can promote wrinkles, depending on its loading position. It is observed

(a)

(b)
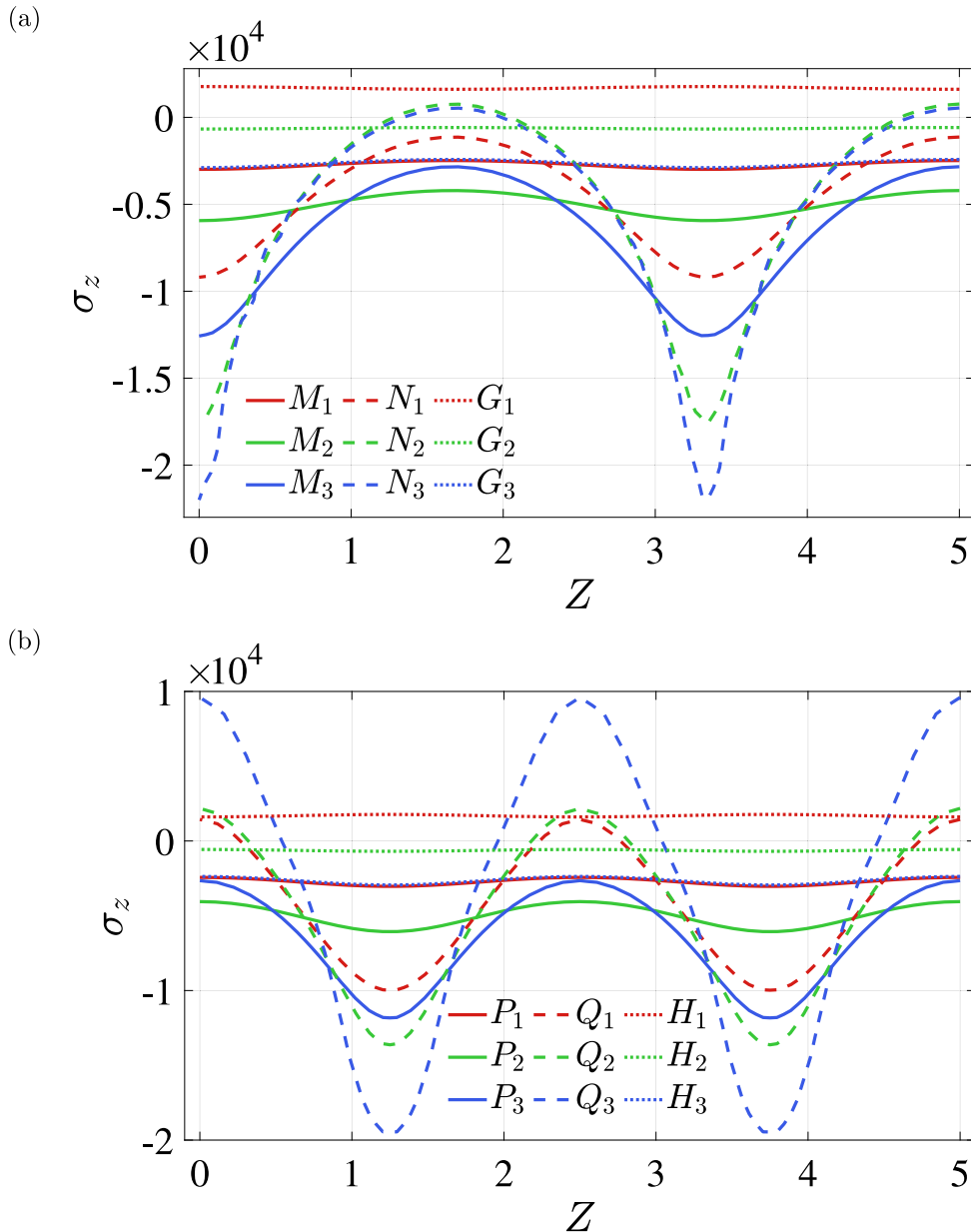
Fig. 20. σ_z distribution of line locating at $X = 0$ on outer surface with radial/aixal electric potential difference: (a) mode 1, at moments M_1–M_3 (solid lines), N_1–N_3 (dashed lines) and G_1–G_3 (dotted lines); (b) mode 2, at moments P_1–P_3 (solid lines), Q_1–Q_3 (dashed lines) and H_1–H_3 (dotted lines).

that residual stresses induced by the growth can be adjusted using an external voltage, leading to a redistribution of stress fields, which can be exploited to remodel the shape. Similar to the results obtained in the analytical solution, the applied voltage in the radial direction reaches the upper limit corresponding to the crash of simulation, resulting from the non-uniformity of the residual stress. In addition, it is also observed that the upper limit decreases with the growth parameter at a constant axial stretch, showing that the growth effect plays an important role in stress redistribution.

To conclude, combining electro-mechanics with growth fields enhances the flexibility of shape morphing schemes for soft materials. The proposed finite element framework using a mixed formulation is promising for capturing the mechanical response of growing electro-elastic solids. The current framework can be used for designing applications in smart devices made of electro-active polymers. The loading cases and material models used in the present

work are relatively simple. Future extensions of this work can focus on incorporating complex loading cases and anisotropic material models to capture additional physics and realize twisting and curling deformations that can aid in the design of versatile smart devices. In addition, the time-dependent response of growing electro-elastic solids is interesting and challenging, which needs to be addressed in future work.

Declaration of competing interest

The authors declare that they have no known competing financial interests or personal relationships that could have appeared to influence the work reported in this paper.

Data availability

No data was used for the research described in the article

Acknowledgements

Appendix A. The first variation of energy function

The first variant of the strain energy function ($\Psi^{\text{mech,dev}} + \Psi^{\text{coup}}$) and the perturbed Lagrangian Ψ_{PL} is given as

$$
\begin{aligned}
\delta \Pi &= \int_{\mathcal{B}_r} \left(\delta F_{iJ} \frac{\partial (\Psi^{\text{mech,dev}} + \Psi^{\text{coup}})}{\partial F_{iJ}} + \delta \bar{\mathbb{E}}_I \frac{\partial (\Psi^{\text{mech,dev}} + \Psi^{\text{coup}})}{\partial \bar{\mathbb{E}}_I} \right) J^g \, \mathrm{d}V \\
&\quad + \int_{\mathcal{B}_r} p \delta J + \delta p \left(J - J^g - \frac{p}{\kappa} J^g \right) \, \mathrm{d}V - \delta \Pi_{\text{ext}} \\
&= \int_{\mathcal{B}_r} \left(\delta F_{iJ} \bar{P}_{iJ} - \delta \bar{\mathbb{E}}_I \bar{\mathbb{D}}_I \right) J^g \, \mathrm{d}V \\
&\quad + \int_{\mathcal{B}_r} p \delta J + \delta p \left(J - J^g - \frac{p}{\kappa} J^g \right) \, \mathrm{d}V - \delta \Pi_{\text{ext}} \\
&= \int_{\mathcal{B}_r} \left(\delta F_{iJ} \left(J^e \bar{\sigma}_{ik} F_{Jk}^{-1} \right) + \left(F_{iI}^e \delta \phi_{,i} \right) \left(J^e F_{Ij}^{e-1} \mathrm{d}_j \right) \right) J^g \, \mathrm{d}V \\
&\quad + \int_{\mathcal{B}_r} p \delta J + \delta p \left(J - J^g - \frac{p}{\kappa} J^g \right) \, \mathrm{d}V - \delta \Pi_{\text{ext}} \\
&= \int_{\mathcal{B}_r} \left(\left(\delta u_{i,j} F_{jJ} \right) \left(J \bar{\sigma}_{ik} F_{Jk}^{-1} \right) + J \mathrm{d}_i \delta \phi_{,i} \right) \, \mathrm{d}V \\
&\quad + \int_{\mathcal{B}_r} p J \delta_{ij} \delta u_{i,j} + \delta p \left(J - J^g - \frac{p}{\kappa} J^g \right) \, \mathrm{d}V - \delta \Pi_{\text{ext}} \\
&= \int_{\mathcal{B}_r} \left(\delta u_{i,j} \left(\bar{\sigma}_{ij} + p \delta_{ij} \right) + \delta \phi_{,i} \mathrm{d}_i \right) J \, \mathrm{d}V \\
&\quad + \int_{\mathcal{B}_r} \delta p \left(J - J^g - \frac{p}{\kappa} J^g \right) \, \mathrm{d}V - \delta \Pi_{\text{ext}} \\
&= \int_{\mathcal{B}_r} \left(\delta u_{i,j} \hat{\sigma}_{ij} + \delta \phi_{,i} \mathrm{d}_i \right) J \, \mathrm{d}V + \int_{\mathcal{B}_r} \delta p \left(J - J^g - \frac{p}{\kappa} J^g \right) \, \mathrm{d}V - \delta \Pi_{\text{ext}}
\end{aligned}
\tag{A.1}
$$

where the relations below are used

$$
\begin{aligned}
\hat{\sigma}_{ij} &= \bar{\sigma}_{ij} + p\delta_{ij}, \\
\delta F_{iJ} &= \delta u_{i,J} = \delta u_{i,j} F_{jJ}, \\
\delta J &= J\delta u_{i,i} = J\delta u_{i,j}\delta_{ij}, \\
\bar{\mathbb{D}}_I &= J^e F_{Ii}^{e-1} \mathrm{d}_i, \\
\bar{\mathbb{E}}_I &= F_{iI}^e \mathrm{e}_i, \\
\bar{P}_{iJ} &= J^e \bar{\sigma}_{ik} F_{Jk}^{-1}.
\end{aligned}
\tag{A.2}
$$

Appendix B. The second variation of energy function

The second variation $d(\cdot)$ of the energy functional ($\Psi^{\mathrm{mech,dev}} + \Psi^{\mathrm{coup}}$) and the perturbed Lagrangian Ψ_{PL} can be written as

$$
\begin{aligned}
&d\left(\delta\Psi^{\mathrm{mech,dev}} + \delta\Psi^{\mathrm{coup}} + \delta\Psi_{\mathrm{PL}}\right) \\
&= \int_{\mathcal{B}_r} d\left[\left(\delta F_{iJ}\bar{P}_{iJ} - \delta\bar{\mathbb{E}}_I\bar{\mathbb{D}}_I\right)J^g + \delta p\left(J - J^g - \frac{p}{\kappa}J^g\right) + p\delta J\right]\,\mathrm{d}V \\
&= \int_{\mathcal{B}_r} \delta F_{iJ}\left(\frac{\partial\bar{P}_{iJ}}{\partial F_{kL}}dF_{kL} + \frac{\partial\bar{P}_{iJ}}{\partial\bar{\mathbb{E}}_K}d\bar{\mathbb{E}}_K\right)J^g \\
&\quad - \delta\bar{\mathbb{E}}_I\left(\frac{\partial\bar{\mathbb{D}}_I}{\partial F_{jK}}dF_{jK} + \frac{\partial\bar{\mathbb{D}}_I}{\partial\bar{\mathbb{E}}_J}d\bar{\mathbb{E}}_J\right)J^g \\
&\quad + \delta p\left(dJ - \frac{dp}{\kappa}J^g\right) + dp\delta J + pd(\delta J)\,\mathrm{d}V \\
&= \int_{\mathcal{B}_r} \delta u_{i,j}F_{jJ}\left(\frac{\partial\bar{P}_{iJ}}{\partial F_{kL}}du_{k,l}F_{lL} - \frac{\partial\bar{P}_{iJ}}{\partial\bar{\mathbb{E}}_K}F_{kK}^e d\phi_{,k}\right)J^g \\
&\quad + F_{iI}^e\delta\phi_{,i}\left(\frac{\partial\bar{\mathbb{D}}_I}{\partial F_{jK}}du_{j,l}F_{lK} - \frac{\partial\bar{\mathbb{D}}_I}{\partial\bar{\mathbb{E}}_J}F_{kJ}^e d\phi_{,k}\right)J^g \\
&\quad + \delta p\left(Jdu_{i,i} - \frac{dp}{\kappa}J^g\right) + dpJ\delta u_{k,k} + p\delta u_{i,j}J\left(\delta_{ij}\delta_{kl} - \delta_{jk}\delta_{il}\right)du_{k,l}\,\mathrm{d}V \\
&= \int_{\mathcal{B}_r} \delta u_{i,j}\left[F_{jJ}\frac{\partial\bar{P}_{iJ}}{\partial F_{kL}}F_{lL}J^g + pJ\left(\delta_{ij}\delta_{kl} - \delta_{jk}\delta_{il}\right)\right]du_{k,l} \\
&\quad - \delta u_{i,j}\left(F_{jJ}\frac{\partial\bar{P}_{iJ}}{\partial\bar{\mathbb{E}}_K}F_{kK}^e J^g\right)d\phi_{,k} \\
&\quad + \delta\phi_{,i}\left(F_{iI}^e\frac{\partial\bar{\mathbb{D}}_I}{\partial F_{jK}}F_{lK}J^g\right)du_{j,l} - \delta\phi_{,i}\left(F_{iI}^e\frac{\partial\bar{\mathbb{D}}_I}{\partial\bar{\mathbb{E}}_J}F_{kJ}^e J^g\right)d\phi_{,k} \\
&\quad + \delta pJdu_{i,i} - \delta p\frac{J^g}{\kappa}dp + \delta u_{k,k}Jdp\,\mathrm{d}V \\
&= \int_{\mathcal{B}_r} \delta u_{i,j}\mathrm{e}_{ijkl}Jdu_{k,l} - \delta u_{i,j}\mathrm{p}_{ijk}Jd\phi_{,k} + \delta\phi_{,i}\hat{\mathrm{p}}_{ijl}Jdu_{j,l} - \delta\phi_{,i}\mathrm{d}_{ik}Jd\phi_{,k} \\
&\quad + \delta pJdu_{i,i} - \delta p\frac{J^g}{\kappa}dp + \delta u_{k,k}Jdp\,\mathrm{d}V
\end{aligned}
\tag{B.1}
$$

where the following relations are used

$$d\left(\delta J\right) = \delta u_{i,j} J \left(\delta_{ij}\delta_{kl} - \delta_{jk}\delta_{il}\right) du_{k,l},$$

$$\mathrm{e}_{ijkl} = J^{e^{-1}} F^e_{jJ} \frac{\partial \bar{P}^A_{iJ}}{\partial F^e_{kL}} F^e_{lL} + p\left(\delta_{ij}\delta_{kl} - \delta_{jk}\delta_{il}\right),$$

$$\mathrm{p}_{ijk} = J^{e^{-1}} F^e_{jJ} \frac{\partial \bar{P}_{iJ}}{\partial \bar{\mathbb{E}}_K} F^e_{kK},$$

$$\hat{\mathrm{p}}_{ijl} = J^{e^{-1}} F^e_{iI} \frac{\partial \bar{\mathbb{D}}_I}{\partial F^e_{jK}} F^e_{lK},$$

$$\mathrm{d}_{ik} = J^{e^{-1}} F^e_{iI} \frac{\partial \bar{\mathbb{D}}_I}{\partial \bar{\mathbb{E}}_J} F^e_{kJ}.$$

References

[1] D. Ambrosi, G.A. Ateshian, E.M. Arruda, S.C. Cowin, J. Dumais, A. Goriely, G.A. Holzapfel, J.D. Humphrey, R. Kemkemer, E. Kuhl, J.E. Olberding, L.A. Taber, K. Garikipati, Perspectives on biological growth and remodeling, J. Mech. Phys. Solids 59 (4) (2011) 863–883.

[2] B. Li, G.-K. Xu, X.-Q. Feng, Tissue–growth model for the swelling analysis of core–shell hydrogels, Soft Mater. 11 (2) (2013) 117–124.

[3] E. Siéfert, E. Reyssat, J. Bico, B. Roman, Bio-inspired pneumatic shape-morphing elastomers, Nature Mater. 18 (1) (2019) 24–28.

[4] M.K. Rausch, E. Kuhl, On the effect of prestrain and residual stress in thin biological membranes, J. Mech. Phys. Solids 61 (9) (2013) 1955–1969.

[5] B. Li, Y.-P. Cao, X.-Q. Feng, H. Gao, Mechanics of morphological instabilities and surface wrinkling in soft materials: a review, Soft Matter 8 (21) (2012) 5728.

[6] Z. Li, J. Wang, M. Hossain, C. Kadapa, A general theoretical scheme for shape-programming of incompressible hyperelastic shells through differential growth, Int. J. Solids Struct. 265–266 (2023) 112128.

[7] Y. Du, Y. Su, C. Lü, W. Chen, M. Destrade, Electro-mechanically guided growth and patterns, J. Mech. Phys. Solids 143 (2) (2020) 104073.

[8] A. Menzel, E. Kuhl, Frontiers in growth and remodeling, Mech. Res. Commun. 42 (2012) 1–14.

[9] S. Budday, P. Steinmann, E. Kuhl, The role of mechanics during brain development, J. Mech. Phys. Solids 72 (2014) 75–92.

[10] F. Xu, C. Fu, Y. Yang, Water affects morphogenesis of growing aquatic plant leaves, Phys. Rev. Lett. 124 (3) (2020) 038003.

[11] S. Wang, N. Demirci, M.A. Holland, Numerical investigation of biomechanically coupled growth in cortical folding, Biomech. Model. Mechanobiol. 20 (2) (2021) 555–567.

[12] B. Dortdivanlioglu, C. Linder, Diffusion-driven swelling-induced instabilities of hydrogels, J. Mech. Phys. Solids 125 (2019) 38–52.

[13] S.A. Chester, C.V. Di Leo, L. Anand, A finite element implementation of a coupled diffusion-deformation theory for elastomeric gels, Int. J. Solids Struct. 52 (2015) 1–18.

[14] Z. Ding, Z. Liu, J. Hu, S. Swaddiwudhipong, Z. Yang, Inhomogeneous large deformation study of temperature-sensitive hydrogel, Int. J. Solids Struct. 50 (16–17) (2013) 2610–2619.

[15] D. Han, C. Farino, C. Yang, T. Scott, D. Browe, W. Choi, J.W. Freeman, H. Lee, Soft robotic manipulation and locomotion with a 3D printed electroactive hydrogel, ACS Appl. Mater. Interfaces 10 (21) (2018) 17512–17518.

[16] F. Zhou, M. Zhang, X. Cao, Z. Zhang, X. Chen, Y. Xiao, Y. Liang, T.-W. Wong, T. Li, Z. Xu, Fabrication and modeling of dielectric elastomer soft actuator with 3D printed thermoplastic frame, Sensors Actuators A 292 (2019) 112–120.

[17] W. Pang, X. Cheng, H. Zhao, X. Guo, Z. Ji, G. Li, Y. Liang, Z. Xue, H. Song, F. Zhang, Z. Xu, L. Sang, W. Huang, T. Li, Y. Zhang, Electro-mechanically controlled assembly of reconfigurable 3D mesostructures and electronic devices based on dielectric elastomer platforms, Natl. Sci. Rev. 7 (2) (2020) 342–354.

[18] E. Hajiesmaili, N.M. Larson, J.A. Lewis, D.R. Clarke, Programmed shape-morphing into complex target shapes using architected dielectric elastomer actuators, Sci. Adv. 8 (28) (2022) eabn9198.

[19] M. Mehnert, M. Hossain, P. Steinmann, A complete thermo–electro–viscoelastic characterization of dielectric elastomers, Part I: Experimental investigations, J. Mech. Phys. Solids 157 (1) (2021) 104603.

[20] M. Mehnert, M. Hossain, P. Steinmann, A complete thermo-electro-viscoelastic characterization of dielectric elastomers, Part II: Continuum modeling approach, J. Mech. Phys. Solids 157 (8) (2021) 104625.

[21] M. Mehnert, M. Hossain, P. Steinmann, On nonlinear thermo-electro-elasticity, Proc. Math. Phys. Eng. Sci. 472 (2190) (2016) 20160170.

[22] Z. Suo, Theory of dielectric elastomers, Acta Mech. Solida Sin. 23 (6) (2010) 549–578.

[23] D.J. Blackiston, K.A. McLaughlin, M. Levin, Bioelectric controls of cell proliferation: Ion channels, membrane voltage and the cell cycle, Cell Cycle 8 (21) (2009) 3527–3536.

[24] M. Levin, Bioelectric mechanisms in regeneration: Unique aspects and future perspectives, Sem. Cell Dev. Biol. 20 (5) (2009) 543–556.

[25] R.H. Funk, T. Monsees, N. Özkucur, Electromagnetic effects – From cell biology to medicine, Prog. Histochem. Cytochem. 43 (4) (2009) 177–264.

[26] M. Levin, Bioelectric signaling: Reprogrammable circuits underlying embryogenesis, regeneration, and cancer, Cell 184 (8) (2021) 1971–1989.

[27] M.P. Harris, Bioelectric signaling as a unique regulator of development and regeneration, Development 148 (10) (2021).

[28] D.-H. Kim, J. Viventi, J.J. Amsden, J. Xiao, L. Vigeland, Y.-S. Kim, J.A. Blanco, B. Panilaitis, E.S. Frechette, D. Contreras, D.L. Kaplan, F.G. Omenetto, Y. Huang, K.-C. Hwang, M.R. Zakin, B. Litt, J.A. Rogers, Dissolvable films of silk fibroin for ultrathin conformal bio-integrated electronics, Nature Mater. 9 (6) (2010) 511–517.

[29] D.-H. Kim, N. Lu, R. Ma, Y.-S. Kim, R.-H. Kim, S. Wang, J. Wu, S.M. Won, H. Tao, A. Islam, K.J. Yu, T.-i. Kim, R. Chowdhury, M. Ying, L. Xu, M. Li, H.-J. Chung, H. Keum, M. McCormick, P. Liu, Y.-W. Zhang, F.G. Omenetto, Y. Huang, T. Coleman, J.A. Rogers, Epidermal electronics, Science 333 (6044) (2011) 838–843.

[30] L. Xu, S.R. Gutbrod, Y. Ma, A. Petrossians, Y. Liu, R.C. Webb, J.A. Fan, Z. Yang, R. Xu, J.J. Whalen III, J.D. Weiland, Y. Huang, I.R. Efimov, J.A. Rogers, Materials and fractal designs for 3D multifunctional integumentary membranes with capabilities in cardiac electrotherapy, Adv. Mater. 27 (10) (2015) 1731–1737.

[31] L.C. Lee, J. Sundnes, M. Genet, J.F. Wenk, S.T. Wall, An integrated electromechanical-growth heart model for simulating cardiac therapies, Biomech. Model. Mechanobiol. 15 (4) (2016) 791–803.

[32] H. Yuk, B. Lu, X. Zhao, Hydrogel bioelectronics, Chem. Soc. Rev. 48 (6) (2019) 1642–1667.

[33] B. Xu, R.C. Hayward, Low-voltage switching of crease patterns on hydrogel surfaces, Adv. Mater. 25 (39) (2013) 5555–5559.

[34] R. Yang, H. Liang, Dynamic electro-regulation of the stiffness gradient hydrogels, RSC Adv. 8 (12) (2018) 6675–6679.

[35] M. Ben Amar, A. Goriely, Growth and instability in elastic tissues, J. Mech. Phys. Solids 53 (10) (2005) 2284–2319.

[36] A. Goriely, M. Ben Amar, Differential growth and instability in elastic shells, Phys. Rev. Lett. 94 (19) (2005) 198103.

[37] A. Goriely, The Mathematics and Mechanics of Biological Growth, in: Interdisciplinary Applied Mathematics, 0939-6047, vol. 45, Springer, New York, 2017.

[38] S. Mehta, G. Raju, P. Saxena, Growth induced instabilities in a circular hyperelastic plate, Int. J. Solids Struct. 226–227 (2021) 111026.

[39] V. Kondaurov, L. Nikitin, Finite strains of viscoelastic muscle tissue, J. Appl. Math. Mech. 51 (3) (1987) 346–353.

[40] E.K. Rodriguez, A. Hoger, A.D. McCulloch, Stress-dependent finite growth in soft elastic tissues, J. Biomech. 27 (4) (1994) 455–467.

[41] E. Kuhl, Growing matter: a review of growth in living systems, J. Mech. Behav. Biomed. Mater. 29 (2014) 529–543.

[42] G.A. Maugin, Continuum Mechanics of Electromagnetic Solids, in: North-Holland Series in Applied Mathematics and Mechanics, vol. 33, North-Holland and Sole distributors for the U.S.A. and Canada Elsevier Science Pub. Co, Amsterdam and New York and New York, N.Y., U.S.A, 1988.

[43] A. Dorfmann, R.W. Ogden, Nonlinear electroelasticity, Acta Mech. 174 (3) (2005) 167–183.

[44] A. Dorfmann, R.W. Ogden, Nonlinear electroelastostatics: Incremental equations and stability, Internat. J. Engrg. Sci. 48 (1) (2010) 1–14.

[45] L. Dorfmann, R.W. Ogden, Instabilities of soft dielectrics, Philos. Trans. Ser. A Math. Phys. Eng. Sci. 377 (2144) (2019) 20180077.

[46] Z. Suo, X. Zhao, W.H. Greene, A nonlinear field theory of deformable dielectrics, J. Mech. Phys. Solids 56 (2) (2008) 467–486.

[47] R.M. McMeeking, C.M. Landis, Electrostatic forces and stored energy for deformable dielectric materials, J. Appl. Mech. 72 (4) (2005) 581–590.

[48] R.M. McMeeking, C.M. Landis, S.M. Jimenez, A principle of virtual work for combined electrostatic and mechanical loading of materials, Int. J. Non-Linear Mech. 42 (6) (2007) 831–838.

[49] X. Zhao, W. Hong, Z. Suo, Electromechanical hysteresis and coexistent states in dielectric elastomers, Phys. Rev. B 76 (13) (2007) 134113.

[50] X. Zhao, Z. Suo, Electrostriction in elastic dielectrics undergoing large deformation, J. Appl. Phys. 104 (12) (2008) 123530.

[51] S. Budday, P. Steinmann, E. Kuhl, Secondary instabilities modulate cortical complexity in the mammalian brain, Phil. Mag. 95 (28–30) (2015) 3244–3256.

[52] S. Budday, S. Andres, B. Walter, P. Steinmann, E. Kuhl, Wrinkling instabilities in soft bilayered systems, Philos. Trans. Ser. A Math. Phys. Eng. Sci. 375 (2093) (2017).

[53] B. Dortdivanlioglu, A. Javili, C. Linder, Computational aspects of morphological instabilities using isogeometric analysis, Comput. Methods Appl. Mech. Engrg. 316 (2017) 261–279.

[54] Y. Yang, H.-H. Dai, F. Xu, M. Potier-Ferry, Pattern transitions in a soft cylindrical shell, Phys. Rev. Lett. 120 (21) (2018) 215503.

[55] M. Holland, S. Budday, A. Goriely, E. Kuhl, Symmetry breaking in wrinkling patterns: Gyri are universally thicker than sulci, Phys. Rev. Lett. 121 (22) (2018) 228002.

[56] A.K. Sharma, M.M. Joglekar, A computationally efficient locking free numerical framework for modeling visco-hyperelastic dielectric elastomers, Comput. Methods Appl. Mech. Engrg. 352 (2019) 625–653.

[57] E. Garcia-Blanco, R. Ortigosa, A.J. Gil, C.H. Lee, J. Bonet, A new computational framework for electro-activation in cardiac mechanics, Comput. Methods Appl. Mech. Engrg. 348 (2019) 796–845.

[58] M. Franke, R. Ortigosa, J. Martínez-Frutos, A.J. Gil, P. Betsch, A thermodynamically consistent time integration scheme for non-linear thermo-electro-mechanics, Comput. Methods Appl. Mech. Engrg. 389 (2022) 114298.

[59] D.K. Vu, P. Steinmann, G. Possart, Numerical modelling of non-linear electroelasticity, Internat. J. Numer. Methods Engrg. 70 (6) (2007) 685–704.

[60] R. Bustamante, A variational formulation for a boundary value problem considering an electro-sensitive elastomer interacting with two bodies, Mech. Res. Commun. 36 (7) (2009) 791–795.

[61] F. Vogel, On the Modeling and Computation of Electro-and Magneto-Active Polymers, Lehrstuhl für Technische Mechanik, Universität Erlangen-Nürnberg, 2015.

[62] E.A. de Souza Neto, D. Perić, M. Dutko, D. Owen, Design of simple low order finite elements for large strain analysis of nearly incompressible solids, Int. J. Solids Struct. 33 (20) (1996) 3277–3296.

[63] D.L. Henann, S.A. Chester, K. Bertoldi, Modeling of dielectric elastomers: Design of actuators and energy harvesting devices, J. Mech. Phys. Solids 61 (10) (2013) 2047–2066.

[64] M. Jabareen, On the modeling of electromechanical coupling in electroactive polymers using the mixed finite element formulation, Procedia IUTAM 12 (2015) 105–115.

[65] D. Bishara, M. Jabareen, A reduced mixed finite-element formulation for modeling the viscoelastic response of electro-active polymers at finite deformation, Math. Mech. Solids 24 (5) (2019) 1578–1610.

[66] J.C. Simo, R.L. Taylor, K.S. Pister, Variational and projection methods for the volume constraint in finite deformation elasto-plasticity, Comput. Methods Appl. Mech. Engrg. 51 (1–3) (1985) 177–208.

[67] F. Brezzi, K.-j. Bathe, A discourse on the stability conditions for mixed finite element formulations, Comput. Methods Appl. Mech. Engrg. 82 (1) (1990) 27–57.

[68] F. Brezzi, M. Fortin, Mixed and Hybrid Finite Element Methods, Vol. 15, Springer Science & Business Media, 2012.

[69] C. Kadapa, M. Hossain, A robust and computationally efficient finite element framework for coupled electromechanics, Comput. Methods Appl. Mech. Engrg. 372 (7) (2020) 113443.

[70] C. Kadapa, W.G. Dettmer, D. Perić, Subdivision based mixed methods for isogeometric analysis of linear and nonlinear nearly incompressible materials, Comput. Methods Appl. Mech. Engrg. 305 (2016) 241–270.

[71] C. Kadapa, M. Hossain, A linearized consistent mixed displacement-pressure formulation for hyperelasticity, Mech. Adv. Mater. Struct. 29 (2) (2022) 267–284.

[72] R.W. Ogden, Non-Linear Elastic Deformations, Dover Publications, 1997.

[73] J. Bonet, R.D. Wood, Nonlinear Continuum Mechanics for Finite Element Analysis, second ed., Cambridge University Press, 2008.

[74] C. Kadapa, Z. Li, M. Hossain, J. Wang, On the advantages of mixed formulation and higher-order elements for computational morphoelasticity, J. Mech. Phys. Solids 148 (2021) 104289.

[75] J. Wang, Z. Li, Z. Jin, A theoretical scheme for shape-programming of thin hyperelastic plates through differential growth, Math. Mech. Solids (2022) 108128652210896.